Forschungszentrum Jülich
*in der Helmholtz-Gemeinschaft*

Institut für Festkörperforschung

# *Barrier and interface properties of magnetic tunneling junctions studied via electrical transport*

*Simon Stein*

Jül-4123

# *Barrier and interface properties of magnetic tunneling junctions studied via electrical transport*

*Simon Stein*

**Berichte des Forschungszentrums Jülich ; 4123**
ISSN 0944-2952
Institut für Festkörperforschung Jül-4123
D 38 (Diss., Köln, Univ., 2004)

Zu beziehen durch: Forschungszentrum Jülich GmbH · Zentralbibliothek
D-52425 Jülich · Bundesrepublik Deutschland
☎ 02461 61-5220 · Telefax: 02461 61-6103 · e-mail: zb-publikation@fz-juelich.de

# Abstract

Magnetic tunneling junctions exhibiting a high resistance change with switching of the magnetization of their electrodes have a high application potential for magnetic random access memories (MRAM) and magnetic field sensors. In this work magnetic tunneling junctions with high tunneling magneto resistance (TMR) values have been fabricated. In contrast to other works the $Al_2O_3$ tunneling barriers in these samples were created with a UV-light enhanced thermal oxidation process which allows for barrier resistances ($R \cdot A$) lying in the range between natural oxidation and conventional plasma oxidation.

To determine barrier and electrode-barrier interface properties the magnetic tunneling junctions were subjected to extended transport characterizations. Structural properties of the layer stack and the barrier were investigated by the use of scanning tunneling microscopy (STM) and transmission electron microscopy (TEM) measurements.

# Zusammenfassung

Magnetische Tunnelkontakte, die beim Ändern der Magnetisierung der Elektroden große Widerstandsänderungen aufzeigen, haben ein hohes Anwendungspotenzial im Bereich der magnetischen Festkörperspeicher (MRAM) und der Magnetfeldsensorik. In der vorliegenden Arbeit wurden magnetische Tunnelkontakte mit hohen Tunnelmagnetwiderstands-Werten hergestellt. Im Gegensatz zu anderen Arbeiten wurde die Tunnelbarriere aus $Al_2O_3$ dabei mit einem thermischen Oxidationsprozess hergestellt, der durch UV-Licht unterstützt wurde. Dadurch konnten Flächenwiderstände ($R \cdot A$) erzielt werden, die im Bereich zwischen den Werten liegt, die bei natürlicher Oxidation oder Plasmaoxidationsprozessen gefunden werden.

Zur Bestimmung der Eigenschaften von Barriere und Barrieren-Elektrodengrenzschicht wurden die magnetischen Tunnelkontakte einer ausgedehnten Transport-Charakterisierung unterzogen. Strukturelle Eigenschaften des Schichtstapels und der Barriere wurden mit Hilfe von Rastertunnelmikroskopie (STM) und Transmissionselektronenmikroskopie (TEM) durchgeführt.

# Contents

# Introduction

The work presented here is placed in the context of magneto electronics. In this field the influence of magnetic properties on electronic micro devices is at the center of interest. Magneto electronics have been investigated in earnest since the discovery of interlayer exchange coupling (IEC) [1] and giant magneto resistance (GMR) [2] in stacks of thin metallic films in the late 1980s. Basic GMR systems consist of two ferromagnetic films separated by a metallic, non-magnetic spacer and through spin-dependent scattering exhibit high resistance changes depending on the relative magnetization of the ferromagnetic layers. GMR stacks were soon applied as field sensors in read heads of hard disk drives and allowed for a significant increase in memory density.

The tunneling magneto resistance (TMR) effect is found in magnetic tunneling junctions, thin film stacks with insulating tunneling barriers placed in between ferromagnetic layers and was first observed in 1975 [3]. The origin of the TMR effect is found in spin-dependent tunneling. Better preparation technologies in the 1990's allowed the fabrication of TMR systems that showed resistance changes interesting for applications [4]. As with GMR systems the TMR effect is applied in magnetic field sensors. A further important application for magnetic tunneling junctions is developed in the field of magnetic random access memories (MRAM). In this memory a bit is represented by the relative magnetization and thus the resistance value of a single magnetic tunneling junction. Prototypes of MRAM chips with 1 MBit of memory capacity have been presented already [5].

The adaptation of MRAMs to conventional memory technology introduces the need to match impedances between the magnetic tunneling junction and the semiconductor peripherical amplifiers. Here, the advantage of the presence of the tunneling barrier comes into play as the barrier resistance can be adjusted over many orders of magnitude, for operating magnetic tunneling junctions the resistance-area product lies between a few $\Omega\mu m^2$ and hundreds of $M\Omega\mu m^2$. In this work a fabrication method is employed - the UV-light assisted thermal oxidation for the fabrication of the tunneling barrier - that results in magnetic tunneling junctions with resistance-area products of the low $k\Omega\mu m^2$ region which fits well with the required CMOS compatible impedances.

To use and to optimize a tunneling barrier prepared this way an understanding of the electronic transport processes is necessary. Defects in the insulator result in localized states that govern different tunneling transport channels. The temperature as well as the bias dependence of the tunneling conductance can be traced to this defect density by studying said dependencies. The resistance change between different magnetization states should also be controlled. Here the interface between electrodes and barrier comes into play, as TMR reducing magnon excitations are generated in this region. Both defect density and interface structure are influenced by the initial thin film composition, but they also can be affected after fabrication with the help of annealing steps. An additional characteristic most important for the use in memory applications is the stability of the barrier under voltage stress. Testing for this allows a look at the life time of magnetic tunneling junctions as well as gives insight to irreversible barrier changes at high bias values.

In chapter 1, a brief overview is given on the principles of tunneling and ferromagnetism, the two fields that govern the behavior of magnetic tunneling junctions. Chapter 2 explains the technological and physical aspects of sample fabrication which mainly involves magnetron sputtering and optical lithography. Special attention is given to the oxidation process of the tunneling barrier as this is a very important aspect of tunneling junction preparation

which influences most of their properties. Some structural characterization of magnetic tunneling junctions was performed in this work which will be shown in chapter 3. The following chapter attends to the transport measurements of the junctions and the characteristics derived thereby.

# Chapter 1

# Theory

## 1.1 Tunneling in solids

The tunneling effect is one of the most obvious deviations of quantum mechanics in solids from classical physics. If two conductors are separated by an insulating barrier a finite current across this barrier can be detected. This would not be explainable in a classic particle picture and the wave-particle nature of electrons has to be taken into account. With this, a current flow through the barrier is explainable by the overlap of electron wave functions on both sides of the insulator. Frenkel [6] and Sommerfeld and Bethe [7] were the first ones to put forward the mechanism behind tunneling in metal-insulator-metal junctions in the 1930s, and experimental evidence of tunneling was clearly visible in superconducting tunneling junctions (as seen in e.g. [8]). More recent overviews of tunneling in solids are found in [9, 10].

A usual set-up for tunneling junctions in solids is achieved by separating two conducting (metal) sheets $M_1$, $M_2$ by a usually 1 to 2 nm thin insulator I. This is called a metal-insulator-metal contact (MIM). In the following a model for this structure will be presented which will consider the MIM-contact in one dimension normal to the metal-insulator interfaces. Fig. 1.1 shows the case of a general barrier I between metals $M_1$ and $M_2$ with Fermi levels $E_{F_1}$ and $E_{F_2}$ respectively. The work functions $W_1$ and $W_2$ are the

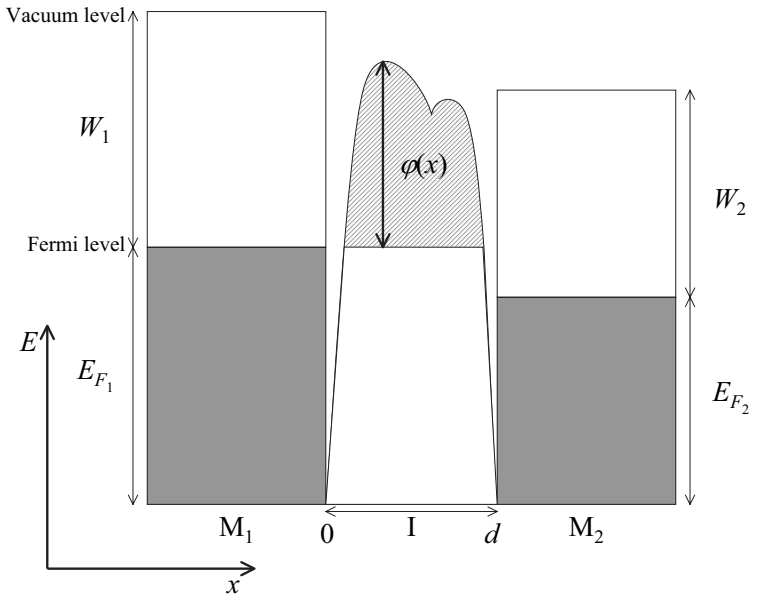


Figure 1.1: *Potential schematic of MIM contact with general barrier.*

energy level required to free an electron from the metal without thermal assistance. The barrier potential is given by $\varphi(x)$. Then the probability $D(E_x)$ of an electron tunneling through the potential barrier in the WKB approximation [11] is:

$$D(E_x) = \exp\left(-\frac{4\pi}{h}\int_0^d \sqrt{2m\left(\varphi(x) - E_x\right)}\, dx\right), \tag{1.1}$$

with $x = 0$ being the starting point of the barrier, $x = d$ being the end point, and $E_x = mv_x^2/2$ as energy component of the tunneling electron in $x$-direction. If $E_x > \varphi(x)$ over the whole barrier, $D(E_x)$ has a periodic solution, the electron is transported through the conduction band of the insulator. In the other case of $E_x < \varphi(x)$ an exponentially decreasing solution is found.

The net tunneling current consists of the difference of currents tunneling from $M_1$ to $M_2$ and vice versa. First, let us consider the current from $M_1$ to $M_2$ solely. If a bias voltage is applied across the barrier the Fermi levels of the electrodes are shifted against each other. A tunneling electron needs to tunnel from an occupied state in $M_1$ to an unoccupied state in $M_2$, which is given by the product of density of states $\rho_1(E)\rho_2(E - eU)$. Apart from

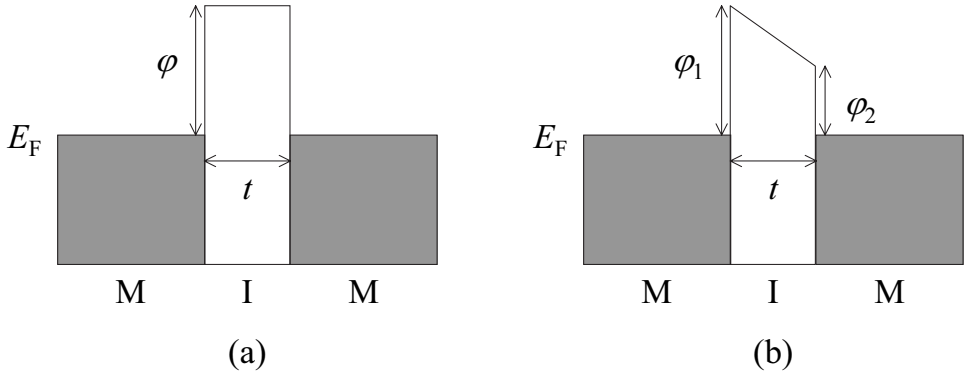


Figure 1.2: *Potential schematic of tunnel barrier models. (a) Simmons model (b) Brinkman model.*

this the tunneling current density $j = I/A$ is proportional to the Fermi distribution $f$ of electrode 1 [10]:

$$j_{1\to 2} \propto \int_{-\infty}^{\infty} \rho_1(E)\rho_2(E - eU)D(E)f(E)\, dE \tag{1.2}$$

The net tunneling current thus results to

$$\begin{aligned} j &= j_{1\to 2} - j_{2\to 1} \\ &= \frac{4\pi}{\hbar}\int_{-\infty}^{\infty} \rho_1(E)\rho_2(E - eU)D(E)(f(E) - f(E - eU))\, dE \end{aligned} \tag{1.3}$$

In the most simple model the barrier can be described by a rectangular potential of height $\varphi$ and width $t$ which was dealt with in [13]. Illustrated in Fig. 1.2a, this would reflect the case when both metals have the same Fermi level $E_F$ and identical interfaces to the insulator. Also the image potential was not included, which when accounted for, rounds off the barrier potential and effectively decreases the height and width. The tunneling probability becomes

$$D(E) = \exp\left(-\frac{2d}{\hbar}\sqrt{2m(\varphi - E)}\right) \tag{1.4}$$

in this simple rectangular model. Simmons [13] continued to develop the resulting current equation for intermediate voltages $eU < \varphi$ finally given as:

$$j = \tfrac{e}{\hbar(2\pi t)^2}\times \tag{1.5}$$

$$\times \left[ \left(\varphi - \tfrac{eU}{2}\right) \exp\left(-\alpha t \sqrt{\varphi - \tfrac{eU}{2}}\right) - \left(\varphi + \tfrac{eU}{2}\right) \exp\left(-\alpha t \sqrt{\varphi + \tfrac{eU}{2}}\right) \right]$$

with $\alpha = 2\sqrt{2m}/\hbar = 1.025/(\text{Å}\sqrt{\text{eV}})$. In [14] this is expanded for $eU \ll \varphi$ in the third power to

$$\begin{aligned} j &= \theta \left(U + \gamma U^3\right) \quad \text{where} \\ \theta &= \left(\frac{e}{h}\right)^2 \frac{\sqrt{2m\varphi}}{t} \exp\left(-\alpha t \sqrt{\varphi}\right), \\ \gamma &= \frac{(\alpha t e)^2}{96\varphi} - \frac{\alpha t e^2}{32} \varphi^{-3/2}. \end{aligned} \tag{1.6}$$

Replacing the natural constants with their numerical values one arrives at the Simmons equation:

$$j = 3.16 \cdot 10^{10} \frac{\sqrt{\varphi}}{t} \exp\left(-1.025 t \sqrt{\varphi}\right) \left[ U + \left( 0.0109 \frac{t^2}{\varphi} - 0.032 \frac{t}{\varphi^{3/2}} \right) U^3 \right] \tag{1.7}$$

Here, the current density is given in $\text{A/cm}^2$, the barrier thickness in Å and the barrier height in eV.

A rectangular barrier only models contacts with equal interface conditions. In practice, even equal electrode materials usually have different interface properties which leads to unequal barrier heights on each side of the insulator. Brinkman [15] accounted for this asymmetry by using a trapezoidal potential barrier model (cf. Fig. 1.2b). This model describes the barrier by the width $d$ and the potential differences $\varphi_1$, $\varphi_2$ at the metal-insulator interfaces. With a potential

$$\varphi(x) = \varphi_1 + \frac{x}{t} \left(\varphi_2 - eU - \varphi_1\right) \tag{1.8}$$

Brinkman arrives at an approximate expression for the conductivity accurate to 10 % for barriers thicker than 10 Å and for $\Delta\varphi/\overline{\varphi} < 1$:

$$\begin{aligned} \frac{G(U)}{G(0)} &= 1 - \frac{A_0 \Delta\varphi}{16\overline{\varphi}^{3/2}} eU + \frac{9A_0^2}{128\overline{\varphi}} (eU)^2, \text{ where} \\ \Delta\varphi &= \varphi_2 - \varphi_1, \; \overline{\varphi} = \frac{\varphi_1 + \varphi_2}{2}, \\ A_0 &= \frac{4\sqrt{2m}t}{3\hbar}, \\ G(0) &= 3.16 \cdot 10^{10} \frac{\sqrt{\overline{\varphi}}}{t} \exp\left(-1.025 t \sqrt{\overline{\varphi}}\right). \end{aligned} \tag{1.9}$$

Integrated this leads to the Brinkman tunneling current equation:

$$j = G(0)\left(U - 0.0213\frac{t\Delta\varphi}{\overline{\varphi}^{3/2}}U^2 + 0.0109\frac{t^2}{\overline{\varphi}}U^3\right). \tag{1.10}$$

Again, the unit of the current density is A/cm$^2$, Å for the barrier thickness, and eV for the barrier height.

## 1.2 Elastic and inelastic tunneling channels

The tunneling current as described above supposes an ideal barrier. To achieve a more accurate description of a real tunneling contact in this section the effect of localized states on the tunneling current will be pointed out. The theories for this transport over localized states were developed for amorphous silicon and will be applied here for the aluminium oxide used as barrier material in this work. Like in the previous section only the one-dimensional case will be examined as it models all relevant processes [16].

Different tunneling channels are distinguished by the number of localized states an electron tunnels over. In order of increasing number $N$ these mechanisms are:

- $N = 0$: *Direct tunneling* as described in section 1.1 where an electron tunnels directly from one electrode to the other. This is depicted in Fig. 1.3a and the current-voltage relation is given by eq. (1.3). The conductivity depends on the barrier thickness $t$ in an exponential manner:

  $$G^{dir} = \hat{G}^{dir} \cdot \exp\left(-2\alpha t\right) \tag{1.11}$$

  with $\alpha^{-1}$ as the localization length. Direct tunneling is the dominant channel in contacts with barriers not much thicker than $\alpha^{-1}$.

  The temperature dependence of $G^{dir}$ is rather weak as it derives from the thermal broadening of the Fermi function of the electrodes [17]:

  $$\begin{aligned} I(T) &= I(0) \cdot \frac{CT}{\sin(CT)} \text{ with} \\ C &= 1.384 \cdot 10^{-4} t/\sqrt{\varphi} \end{aligned} \tag{1.12}$$

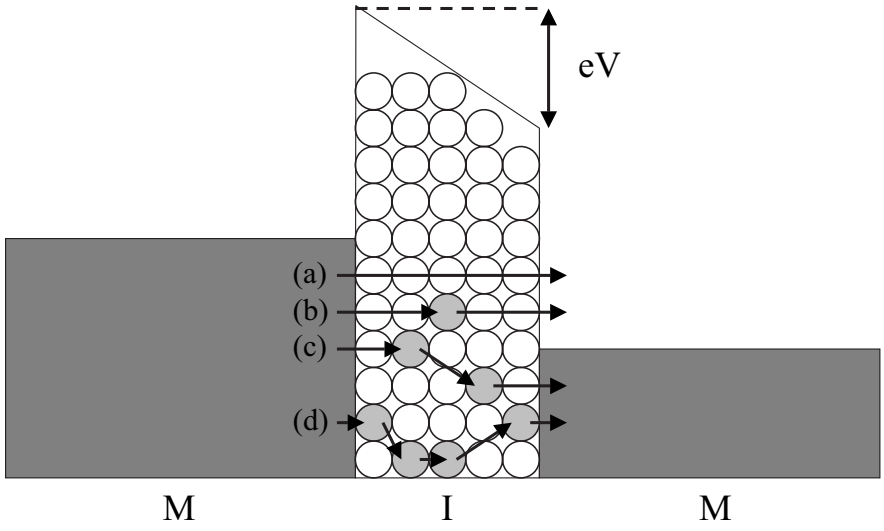


Figure 1.3: *Tunneling channels: (a) direct tunneling with $N = 0$ localized states; (b) resonant tunneling with $N = 1$ localized states; (c) (inelastic) tunneling over $N > 1$ localized states; (d) variable range hopping over "many" localized states.*

with the barrier width $t$ in Åand the barrier height $\varphi$ in eV.

- $N = 1$: *Resonant tunneling.* Here an elastic electron tunnels over one localized state (cf. Fig. 1.3b). The tunneling process is accomplished by an electron first tunneling to the localized state and then continuing to the second electrode. This allows for a much higher barrier thickness. The highest probability for a tunneling process in this case is given for a localized state placed in the middle of the barrier at an energy within an intrinsic width from the Fermi level [16].

  Larkin and Matveev [18] perceived the resonant tunneling conductivity as the sum of all resonant tunneling channels over the contact area. From their calculations and from [19] the barrier thickness dependence of the conductivity can be taken:

$$G^{res} = \hat{G}^{res} \cdot \exp\left(-\alpha t\right). \tag{1.13}$$

  A direct consequence of this thickness dependence is the domination

of the resonant tunneling conductivity over direct tunneling at high barrier thicknesses $t$.

Resonant tunneling is independent of temperature in first approximation. However, electron-phonon interaction leads to a small temperature-dependent correction [20]. Theoretically, resonant (elastic) tunneling should be possible over more than one localized state at even higher barrier thicknesses which is discussed in [18, 21]. However, experiments show that inelastic tunneling created by phonon-assisted hopping prevents these channels from being observed.

- $N > 1$: *Inelastic hopping.* If more than one localized states lie in a tunneling barrier, inelastic transport processes take place. Glazman and Matveev investigated these tunneling processes in [22]. For two localized states they assumed both of them to couple elastically to the electrodes only. Between them coupling occurs inelastically due to electron-phonon interaction (cf. Fig. 1.3c).

  For small voltages $eV \ll k_B T$ Glazman and Matveev arrived at

  $$G_2^{hop} \propto T^{4/3} \cdot \exp\left(-2\alpha t/3\right). \tag{1.14}$$

  Similarly, in the high voltage and low temperature limit $eV \gg k_B T$ the voltage dependence

  $$G_2^{hop} \propto U^{4/3} \cdot \exp\left(-2\alpha t/3\right) \tag{1.15}$$

  is found.

  The fact that the configuration for two localized states is more difficult to find than for resonant tunneling is compensated by the exponentially larger conductivity.

  For the case of $N > 2$ localized states a generalization is possible and the low-bias limit yields the dependence

  $$G_N^{hop} \propto T^{N-[2/(N+1)]} \cdot \exp\left(\frac{-2\alpha t}{N+1}\right) \tag{1.16}$$

respectively the high-bias and low temperature limit

$$G_N^{hop} \propto U^{N-[2/(N+1)]} \cdot \exp\left(\frac{-2\alpha t}{N+1}\right). \tag{1.17}$$

- *Variable range hopping.* As the barrier thickness approaches the bulk limit which is characterized by the variable range hopping length $l_{VRH}$ one-dimensional tunneling channels are no longer possible. The Mott hopping model [23] describes the transport in this case (schematically in Fig. 1.3d). $l_{VRH}$ is determined by two counteracting conditions. On one hand the localized states must be near enough to allow overlap between the electron wave functions. On the other hand the distance between states needs to be high enough to allow for finding a localized state with a small energy difference. The temperature dependent optimum is

$$l_{VRH} = \alpha^{-1} \left(T^\star/T\right)^{1/4} \tag{1.18}$$

where $T^\star$ is given by $k_B T^\star = 23/(g\alpha^3)$ [16]. The Mott hopping model thus results in the following conductivity law:

$$G^{VRH} \propto \exp\left[-\left(T^\star/T\right)^{1/4}\right]. \tag{1.19}$$

In summary, the total conductivity of a tunneling contact consists of the sum of the individual tunneling channels:

$$G(T) = G^{dir}(T) + G^{res}(T) + \sum_{i=2}^{N} G_i^{hop}(T) + G^{VRH}(T). \tag{1.20}$$

## 1.3 Inelastic electron tunneling spectroscopy

Inelastic electron tunneling spectroscopy (IETS) was first used in 1966 [24] and details are found in [10]. Based on transport measurements IETS allows a view on barrier properties. It is based on inelastic tunneling processes which can be caused by localized states in the tunneling barrier (as described above) but also by different excitations inside the barrier or at the barrier/electrode

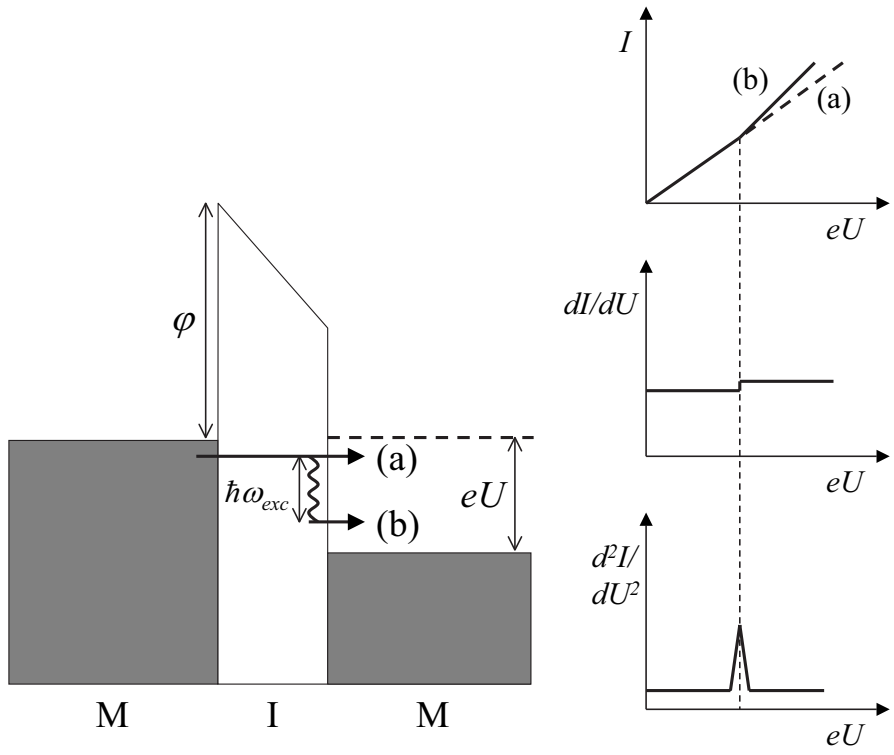


Figure 1.4: *Inelastic electron tunneling spectroscopy. Left: Schematic of Metal-Insulator-Metal contact and (a) elastic tunneling channel, (b) inelastic tunneling channel. $\varphi$ barrier height, $U$ bias voltage, $\hbar\omega_{exc}$ excitation energy. Right, from top to bottom: Schematics of current-voltage graph for elastic and inelastic tunneling current, differential conductivity for inelastic tunneling current, second derivative of current-voltage graph for inelastic tunneling current.*

interface. There are phonon and magnon contributions from barrier and electrodes as well as electronic and vibrational excitations of molecules inside the barrier or the interfaces.

An inelastic excitation of energy $E_{exc} = \hbar\omega_{exc}$ can only take place if the bias voltage $U$ is high enough, i.e. $U = \hbar\omega_{exc}/e$. Since at this excitation bias the additional inelastic tunneling channel is possible, it gives an addition to the total tunneling probability which increases the differential conductivity $dI/dU$ at this bias voltage. As these changes in the differential conductiv-

ity are usually smaller than 2% [25], the second derivative of the tunneling current $d^2I/dU^2$ is measured, where the inelastic excitation will appear as a peak at the energy $\hbar\omega_{exc}$ (cf. Fig. 1.4).

In ferromagnetic tunneling junctions which will be described in detail in chapter 1.6 IETS allows the observation of spin-dependent excitations at the barrier-electrode interface. The relative magnetization of the electrodes alone will cause a change in the IET spectrum as there are spin-dependent inelastic processes, e.g. magnon-assisted inelastic tunneling. This normally causes the antiparallel spectrum to be larger than the parallel spectrum. A basic feature should be a peak at 115 mV for a stretching mode of $Al_2O_3$. Around 20 mV, electrical magnon excitations as well as possible transverse phonon modes that via electron-phonon interaction can cause spin-flips. Thermally excited magnons will be found at room temperature at 25 mV [26, 27].

## 1.4 Ferromagnetism in thin films

Ferromagnetism is a property of materials which show a spontaneous ordering of magnetic moments. The magnetic moment of an atom results from its electrons' non-zero orbital angular momenta and the spin of the electrons. Its value in the ground state of an atom can be derived from the Pauli principle and Hund's rules.

In a solid the magnetic moment of individual atoms is usually reduced. This is caused by breaking of the electron potential symmetry by the crystal field and the delocalization of the conduction electrons. Only $d$ electrons contribute partially and the strongly localized $f$ electrons completely to the orbital momentum. Therefore magnetic solids are not common. Metals in the $3d$ row (Cr, Mn, Fe, Co, Ni) and some $4f$ elements (Gd, Dy) as well as $5f$ elements show magnetic ordering.

The magnetic ordering may add up to a net magnetization density for the solid (the so-called spontaneous magnetization) in which case the ordered state is called *ferromagnetic*. If the local moments sum to zero the ordered

state is called *antiferromagnetic*.

The ordering vanishes above a critical temperature $T_c$ which is known as Curie temperature in ferromagnets and the Néel temperature (often $T_N$) in antiferromagnets.

The term *exchange interaction* describes the sum of the electron-electron interaction through the Pauli principle, Hund's rules, and the crystal interaction. The resulting exchange energy $E_{ex}$ is visible in the lowering of the energy scheme of the density of states $n(E)$ for one spin direction against the other and it follows that $n_\uparrow(E) = n_\downarrow(E - E_{ex})$. The density of states in $3d$ metals is illustrated in Fig. 1.5.

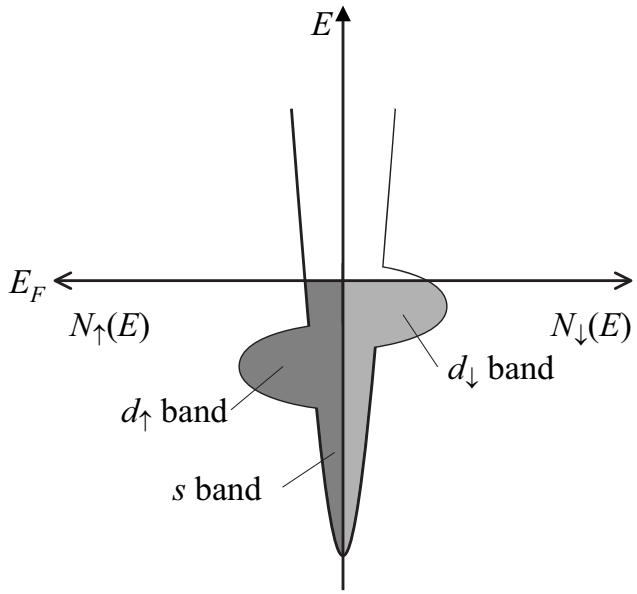


Figure 1.5: *Schematic of density of states for ferromagnetic* $3d$ *metals. Plotted bands refer to* $4s$ *and* $3d$ *bands.*

Above, it was said that in the case of the $3d$ ferromagnets only the $d$ electrons contribute to the magnetic moment. In the band model this is no longer true as hybridization takes place with the delocalized $s$ and $p$ electrons which are the main conduction electrons. Since $s$ and $p$ electrons have large $k$-vectors the Mott two current model is plausible which postulates that the electrons with different spin form separate currents and can be treated in the

free electron approximation [28].

The spin polarization

$$P := \frac{N_\uparrow(E_F) - N_\downarrow(E_F)}{N_\uparrow(E_F) + N_\downarrow(E_F)} \tag{1.21}$$

is the measure of the fraction of majority spin carriers at the Fermi level. It was first treated in ferromagnet/insulator/superconductor contacts [29] where the spin polarization could be measured through the tunneling probability to the Zeeman split quasi-particle density of states of the superconductor. Table 1.1 shows the spin polarization of the $3d$ ferromagnetic metals and some special alloys.

| Material | Ni | Co | Fe | $Ni_{80}Fe_{20}$ | $Co_{50}Fe_{50}$ |
|---|---|---|---|---|---|
| Polarization | 33% | 42% | 44% | 48% | 55% |

Table 1.1: *Spin polarization of 3d ferromagnetic metals and alloys [30]. Measured with the help of Zeeman splitting of energy gap in planar superconductor/$Al_2O_3$/ferromagnet junctions.*

In thin films magnetism is strongly influenced by the surfaces. This gives rise to differences to the bulk ferromagnet in anisotropies and magnetization. The Curie temperature decreases with decreasing film thickness whereas the magnetic moment is increased when compared to bulk values [31].

The magnetic anisotropy is the contribution to the free energy $F$ that depends on the direction of the magnetic moment. The so-called *easy axis* of a ferromagnet which defines the direction of magnetization inside a homogenously magnetized ferromagnet is found at the absolute minima of the free energy. In thin films the magnetic anisotropy is determined mainly by form anisotropy which favors magnetization inside the film plane and which is caused by dipole-dipole interaction [32]. A further but smaller contribution to the magnetic anisotropy is the crystalline anisotropy [33] which is caused by spin-orbit coupling and is found virtually in every at least partially ordered ferromagnet. Thus, in single crystalline Fe the direction of the spontaneous

magnetization lies along the (100) axis. Crystalline easy axes were usually induced in this work by the magnetrons present in the sputtering system.

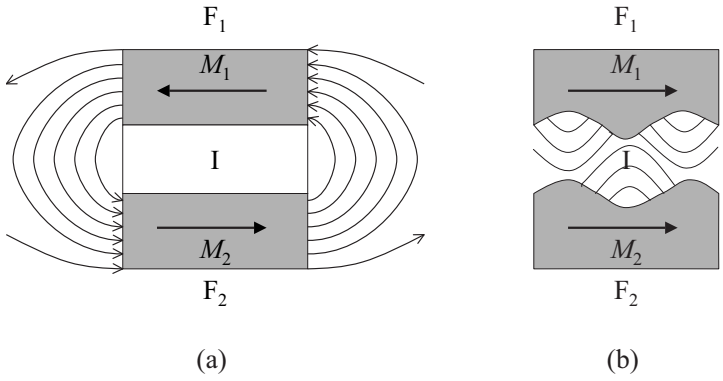


Figure 1.6: *Dipolar coupling in tunnel junctions: (a) Antiferromagnetic stray field coupling (b) Roughness induced ferromagnetic Néel coupling.*

If magnetic thin films are separated by metallic or insulating spacers of a few Angstroms of thickness magnetic coupling effects appear. In metallic systems like Fe/Cr/Fe [1] antiferromagnetic 180 ° and 90 ° coupling between the layers are found. They are caused by an intrinsic mechanism, the interlayer exchange coupling [34, 35]. However, this coupling is not important for tunneling systems which use insulating spacers between the ferromagnetic films. Here, dipolar coupling is present which emerges primarily in two forms. On one hand stray fields at the film edges try to align the films antiferromagnetically, analogous to bulk rod magnets (cf. Fig. 1.6a). On the other hand a rough surface at the interface to the spacer can lead to magnetic field lines leaving the film. If the spacer is thin enough, as in tunneling systems, these field lines can interact with the other film leading to ferromagnetic coupling (so-called orange peel or Néel coupling, cf. Fig. 1.6b) [36].

## 1.5 Exchange-bias effect

As said above antiferromagnetically ordered materials have a zero net magnetization below their order temperature $T_N$. Microscopically this is achieved

by a periodic ordering of the magnetization density. Ideally an antiferromagnet shows pairwise opposite electron spins at the lattice sites.

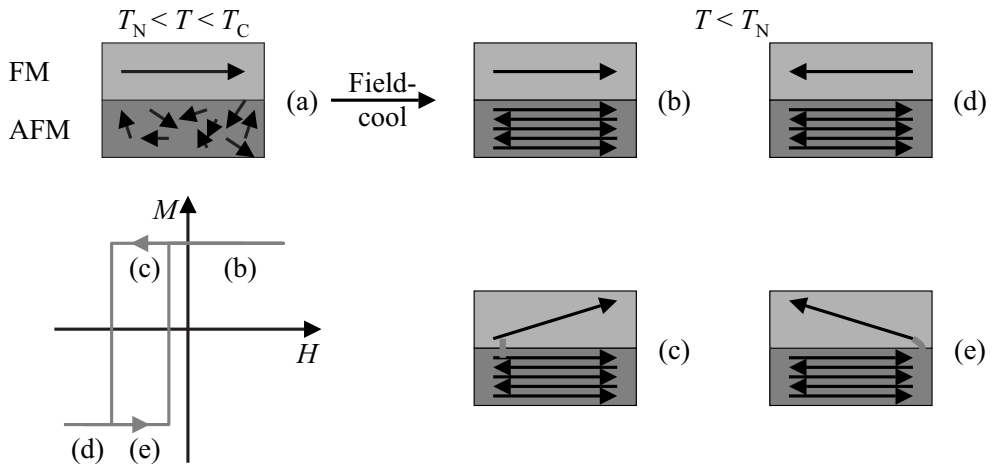


Figure 1.7: *Schematic of magnetization in exchange bias system and corresponding hysteresis curve. (a) Exchange-bias system with unordered antiferromagnet (AFM); (b)-(e) with ordered antiferromagnet at different applied fields.*

If a ferromagnet is in direct contact with an antiferromagnet an unidirectional anisotropy is observed in the hysteresis of the ferromagnet (cf. Fig. 1.7). This was first found in oxidized Co clusters where antiferromagnetic CoO covered the ferromagnetic Co [37]. The hysteresis of the ferromagnet is shifted by an amount $H_{eb}$, the exchange-bias field. The remagnetization of the ferromagnetic film opposite to the anisotropy leads to so-called frustrated spins at the interface which are only switched at a higher value of the external field. This exchange-bias effect allows to pin a ferromagnetic film in the direction of the anisotropy for large field values which very effectively separates the coercive fields of the two different ferromagnetic electrodes in a magnetic tunneling junction (see below).

The exchange-bias effect at first glance can be explained by the energy of the non-compensated antiferromagnet spin structure at the interface [38]. Since this energy accounts for an exchange energy, which is higher by a

factor of 100, interface roughness has to be considered leading to a partial spin frustration and thus to reduced exchange energy [39, 40].

Similar to the reduction of the Curie temperature of a ferromagnet the Néel temperature $T_N$ of an antiferromagnet is reduced in a thin film to the Blocking temperature $T_B$ [41, 42].

## 1.6 Spin-dependent tunneling

When using ferromagnetic electrodes in a tunneling junction one arrives at a magnetic tunneling junction (MTJ). Here, Mott's two current model must be taken into account for the tunneling current. Both spin currents are treated in the free electron approximations and are supposed to be independent of each other.

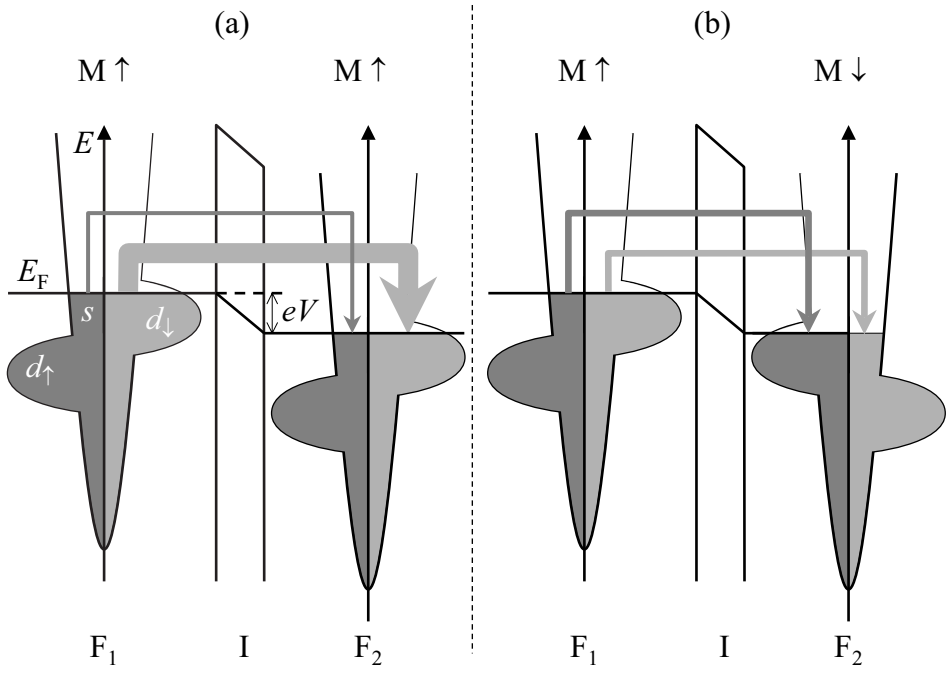


Figure 1.8: *Spin-dependent tunneling in a magnetic tunneling junction. (a) Magnetization of electrodes is parallel to each other. (b) Magnetization of electrodes is antiparallel to each other.*

If it is supposed that the electron spin is conserved during tunneling and that the ferromagnetic electrodes are completely spin polarized (i.e. $P = 1$) an electron of electrode 1 can only tunnel to electrode 2 if the electrodes are magnetized parallel to each other. Fig. 1.8 illustrates this. There are only free states (for the majority spin electrons) in the parallel case whereas in the antiparallel alignment there is no tunneling current. Thus the tunneling current depends on the relative magnetization of the electrodes. The relative change of the resistance of the tunneling junction

$$TMR := \frac{R_{ap} - R_p}{R_p} = \frac{\Delta R}{R} \tag{1.22}$$

between the antiparallel (ap) and parallel (p) magnetization of the electrodes is called tunneling magneto resistance (TMR). Obviously, this value amounts to infinity in the case of $P = 1$. In the case of non-complete spin polarization, a simple model was proposed by Jullière in [3]. It applies only at low temperatures and only gives a dependence of the TMR on spin polarization of the electrodes. Here, the TMR value is given by

$$TMR = \frac{2P_1P_2}{1 - P_1P_2} \tag{1.23}$$

with $P_1$, $P_2$ being the spin polarizations of the ferromagnetic electrodes respectively. In this model basic characteristics of the dependence of junction resistance against applied magnetic field are explained. As long as the electrodes are magnetized parallel to each other the tunneling electrons can tunnel to free $d$ states near the Fermi level on the other side of the barrier which leads to a high current or low junction resistance $R_p \propto \left(N_1^{\uparrow}N_2^{\uparrow} + N_1^{\downarrow}N_2^{\downarrow}\right)^{-1}$. If an external field is swept to a value where one of the electrodes can be magnetized to the opposite direction, the number of free $d$ states is reduced because the corresponding spin sub-band is occupied. Although the other sub-band has free states the number of occupied states of the left electrode is reduced leading to the higher junction resistance $R_{ap} \propto \left(N_1^{\uparrow}N_2^{\downarrow} + N_1^{\downarrow}N_2^{\uparrow}\right)^{-1}$. A complete hysteresis loop is shown in Fig. 1.9.

To explain tunneling behaviour in MTJs more accurately, several other factors have to be taken into account. Slonczewski [43] calculated the TMR

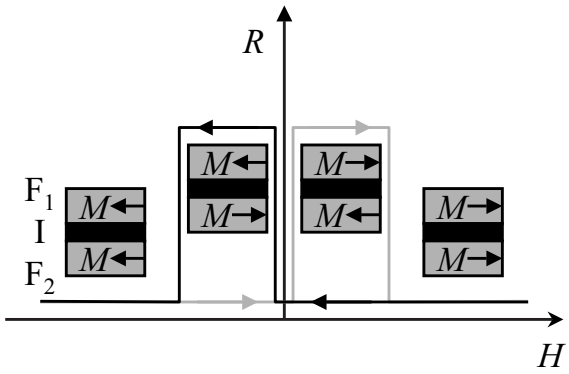


Figure 1.9: *Tunnel magneto resistance: Dependence of resistance on relative magnetization of electrodes in ferromagnet/insulator/ferromagnet ($F_1/I/F_2$) magnetic tunneling junction.*

including a parabolic band structure of the ferromagnetic electrodes. With a simple rectangular barrier potential he arrived at an effective spin polarization of an electrode of

$$P_{eff} = \frac{k_\uparrow - k_\downarrow}{k_\uparrow + k_\downarrow} \cdot \frac{\kappa^2 - k_\uparrow k_\downarrow}{\kappa^2 + k_\uparrow k_\downarrow}, \tag{1.24}$$

where $\kappa := \sqrt{2m(\varphi - E_F)/\hbar}$ is the wave vector inside the barrier, $\varphi$ is the barrier height, $m$ the electron mass, and $k_\uparrow$, $k_\downarrow$ the wave vectors for spin-up respectively spin-down electrons in the electrodes. It follows that in this model the polarization depends on the barrier height which was evaluated numerically in [44]. There it was found that the polarization also depends on the barrier thickness. Discrepancies with experimental data remains since the assumption of a parabolic band structure still is no good model of realistic band structures.

Two other dependencies, on bias voltage and temperature, were not included in the mentioned models. Experiments show that generally the TMR value decreases with increasing bias voltage and increasing temperature.

The voltage dependence of the TMR is in discussion and several causes have been postulated. In this group experiments pointed to a dependence on the number of localized states in the barrier [47]. Others pointed out

bias caused shift of the conduction bands of the ferromagnetic electrodes [30], the influence of a localized state inside the barrier [45], or scattering by magnon excitations [30, 46]. The latter occurs by the creation or destruction of spin-1 magnons which accompanied by a spin-flip process of the partaking electron. An electron after a spin-flip tunnels into the opposite spin sub-band, thus contributing to an inverse TMR effect. With an increase of electron-magnon scattering with increased bias voltage the decrease of the TMR can be explained.

A special voltage dependence of magnetic tunneling junctions is found around zero bias and is aptly called the zero-bias-anomaly. At voltages less than $\pm 150$ mV the resistance of a magnetic tunneling junction decreases sharply, an example can be seen in Fig. 4.11b. Mechanisms like transport over paramagnetic impurities at the interface or metallic impurities in the barrier are supposed to be spin-independent and they are restricted to much smaller bias voltages in the millivolt range so that they are not likely to cause these zero-bias anomalies. Zhang [46] proposed that itinerant tunnel electrons with excess energies above the Fermi level, known as *hot electrons* are responsible for this behavior. This is likely since the zero-bias anomaly ranges over energies up to the order of magnetic excitations. Hot electrons produce magnons at the barrier-electrode interface by collective excitations of local spins which decreases the effective spin polarization at the interface and thus the magneto resistance.

The temperature dependence of the TMR results from two contributions. The first is the influence of the non-magnetic temperature dependence of the tunneling process which was explained above and which together with the spin-dependent part of the conductance leads to an expression of the form [48]

$$G = G^{dir}(T) + G^{dir}(T)\left[P_1(T)P_2(T)\cos(\theta)\right] + G^{rest}(T). \tag{1.25}$$

Here, $G^{dir}$ is the direct, elastic tunneling current from above and $G^{rest}$ is the sum of other contributing tunneling channels. It is supposed that the non-direct tunneling channels do not show spin-dependent tunneling. $\theta$ describes

the angle between the direction of magnetizations of both electrodes. The temperature dependence of the spin polarization was measured by Meservey and Tedrow [49]. They found a dependence of the form

$$P(T) = P_0 \cdot \left(1 - \alpha T^{3/2}\right) \tag{1.26}$$

with $\alpha$, the so-called spin wave parameter, being a material dependent parameter. The explanation for this behavior is the above mentioned magnon excitation at the electrode-barrier interface. Since spin-flip scattering is an inelastic process, the fraction of electrons contributing to the inverse TMR increases with higher temperatures [50].

## 1.7 Reliability of tunneling junctions

If a tunneling junction is subjected to high voltages physical degradation takes place. This can lead to a complete break-down and subsequent short-cutting of a tunneling barrier. To evaluate the voltage reliability and life time of a tunneling barrier, reliability concepts from $SiO_2$ gate oxides can be applied.

The reliability of $SiO_2$ dielectrics for the use in CMOS transistors has been studied for some time [51, 52] and recently these concepts have been applied to $Al_2O_3$ in magnetic tunneling junctions [53]. Electrons tunneling through $SiO_2$ generate traps which there is explained by two different models: In the first the tunneling electron releases its energy upon arrival in the second electrode. This energy generates holes which - alone or together with conduction electrons - tunnel back into the oxide and so generate defects [54]. In the second model the electron energy releases hydrogen atoms present at the interface between barrier and electrode. The hydrogen atoms move through the oxide and cause defects [55]. In both models the creation of defects derives from a present current of electrons and is *not* dependent on the bias voltage. If the defect density reaches a critical value $D_{ot,crit}$ neighboring defects over the whole barrier overlap and allow conduction between each

other and the barrier will break down. This is known as percolation model of break-down [51].

The critical value of defect density is a statistical variable as well as the correlated time-to-breakdown $t_{BD}$. The distribution function for this kind of weakest link process, the Weibull distribution function [59], is given by:

$$F(t) = 1 - \exp\left[-\left(\frac{t}{\eta}\right)^{\beta}\right] \tag{1.27}$$

where $F$ is the cumulative fraction of junctions with break down, $\beta$ is the so-called Weibull slope and $\eta$ the scale factor of the distribution. $F(t)$ gives the probability that a device has broken down by the time $t$. Usually $\ln(-\ln(1-F))$ will be plotted against $\ln(t)$ as this will yield a straight line with slope $\beta$:

$$\ln(-\ln(1-F)) = \beta(\ln(t) - \ln(\eta)). \tag{1.28}$$

The Weibull distributions of junctions with different areas $A_1$, $A_2$ should show equal Weibull slopes $\beta$ and shift vertically by $\ln(A_2/A_1)$. If this is the case the oxide break-down sites are distributed randomly and the break-down does not occur due to perimeter effects [56].

Before break-down takes place in a junction with constant voltage impression, current jumps have been observed. The time $t_i$ after which these jumps of magnitude $\Delta I_i$ occur can be analyzed to give information on voltage stress caused trap generation in the barrier. In $SiO_2$ capacitors, it was found that $t_i$ is Weibull distributed with a Weibull slope $\beta$ that decreases with decreasing $\Delta I_i$ which was explained with a two-trap percolation model. If however pre-break-down steps occur due to the generation of only one trap the Weibull slopes should remain constant with for different $\Delta I_i$.

If the percolation concept is applied to this one-trap case, it is possible to find a relation between the current step values and the trap position in the barrier which is given by $x_{perc}$, the longest distance from the trap to an interface. Das in [57] found the relation between $x_{perc}$ and $D_{ot}$ to be given over

$$\frac{2x_{perc}}{t} - 1 = \frac{1}{AtD_{ot}} \tag{1.29}$$

where $t$ is the barrier thickness, $A$ the junction area, and $D_{ot}$ the density of traps. With $D_{ot}$ given by this relation, at least one trap can be found within $x < x_{perc}$. The connection of trap density and stress time is given by

$$D_{ot} = Ct^m \tag{1.30}$$

where $C$ is a constant that can be fitted from the break-down limit and where the exponent $m = \beta$ for the case of single trap generation. If the data of $t(\Delta I)$ is measured the relation between current step values and trap position is established.

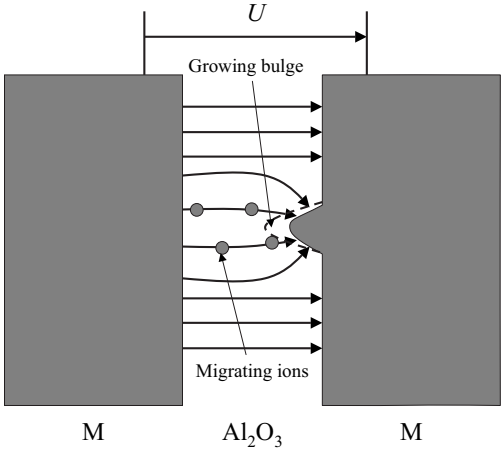


Figure 1.10: *Schematic lateral view of electrical field lines inside a tunneling barrier with roughness-induced bulge. Metal ions migrating from the left to the right electrode follow field lines and concentrate on the bulge in a self-reenforcing process.*

Gundlach [58] proposed a different model for $Al_2O_3$ break-down which took metal ion migration through the barrier as break-down mechanism. Taking the non-ideal, rough barrier into consideration there are bulges and dents at the barrier-electrode interface which leads to a concentration of the electrical field at these places. If the applied voltage is high enough to allow electrode metal ion migration from the positive to the negative side these ions will follow the field lines and gather at the points of highest electrical field, the bulges into the oxide (cf. Fig. 1.10).

This process of growing bulges inside the barrier leading to a break-down is supposed to start at field values of around $10^7$ V/cm which fits with the usual break-down voltages of around 1.1 V in this work ($F = U/d =$ 1.1 V/1.6 nm $\approx 7 \cdot 10^6$ V/cm). However, the time scale of the proposed mechanism is several orders of magnitude higher than that observed during constant voltages stress measurements (cf. chapter 4.6). Where Gundlach saw break-down after tens of seconds, break-down in tunneling barriers produced in this work lasted for tens of minutes (cf. Fig. 4.17) at comparable or higher field values. Reduced barrier roughness of samples in this work (cf. Fig. 3.6 where pits in the $Al_2O_3$ show profiles with radii of around 10 nm and depths of around 0.4 nm) when compared to Gundlach's work (where the assumption is that bulges have a depth-to-radius ratio of more than 1) can explain this change and make the aforementioned models more suited to the data obtained.

# Chapter 2

# Sample preparation

For the fabrication and characterization of thin film tunneling junctions several technologies were employed which are outlined below. For the production of the samples a combined deposition and patterning process was utilized, including sputter deposition, ion beam etching, and optical lithography. The crucial point of the fabrication of the tunneling junctions is the barrier. It needs to be of homogenous thickness, pinhole free, and is usually only 1 to 2 nm thin to allow a sufficiently high tunneling current. Instead of direct deposition of the insulating barrier material, experience has shown that deposition of a metal and subsequent oxidation yield the best results. The cause of this behavior is the wetting effect of aluminium on several transition metals which leads to a decreased roughness of a thin film stack after aluminium is deposited [60]. For the oxidation of the tunneling barrier an optimized process had to be developed.

The characterization was conducted through transport and structural measurements. Transport properties were observed via current-voltage measurements and their (measured or calculated) derivatives. These measurements could be recorded under the influence of magnetic fields or lowered temperatures. Some structural characteristics were performed by scanning tunneling microscopy (STM) and transmission electron microscopy (TEM).

## 2.1 Sputter deposition

The term "Sputtering" was first used in the 1920s by I. Langmuir, and K.H. Kingdon and derives from Latin "sputare" (to emit saliva with noise) [61]. It describes a deposition process that was originally discovered about 150 years ago by Grove (1852) and Plücker (1858) where high energetic particles are generated which erode the surface of a target. The particles are usually positive ions that are accelerated in an electrical field and that are created in a plasma previously.

Choosing the bias so that the target is the cathode of this set-up positive ions remove atoms, molecules, or clusters from the surface of the target which are dispersed in the sputtering system. If a substrate is placed near the target, a substantial amount of the eroded target material will deposit there and form a continuous film.

The plasma used for sputter deposition is created by applying a voltage in a diode configuration between the cathode (target) and the anode (substrate). A gas atmosphere, usually Argon for non-reactive sputtering, with partial pressures ranging from some $10^{-4}$ to 1 mbar is brought into the diode chamber that needs to have residual gas pressures much lower than the Ar pressure. From a certain voltage threshold on the plasma is ignited. Since recombination of gas ions and electrons takes place this is visible by a discharge glow.

Usually the cathode is enhanced by a ring of permanent magnets positioned above it. These magnets are placed as to keep the charged particles in a ring-formed area near the target. This increases the charge carrier density, allows for higher sputtering rates, and also makes lower sputtering gas pressure possible. This principle is the so-called magnetron sputtering [62]. The geometry and electron motion of magnetron sputtering is shown in Fig. 2.1.

When employing a dc voltage between target and substrate only conductive targets can be used as insulating materials would build up a positive charge which counteracts the applied voltage. To deposit non-conducting

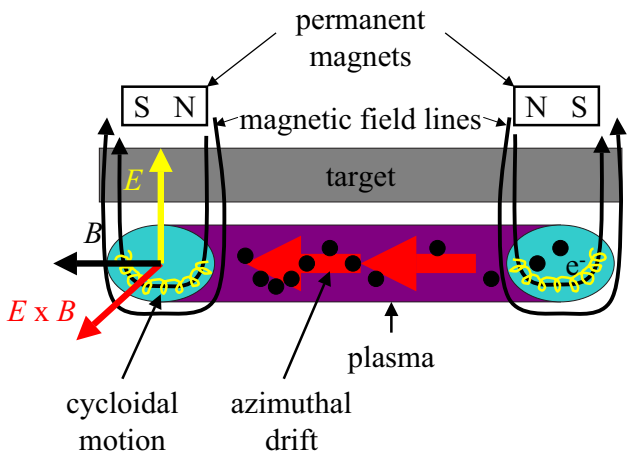


Figure 2.1: *Geometry and electron motion of magnetron sputtering.*

materials an ac field in the radio frequency range is used for plasma generation, usually with the industry standard frequency of $f = 13.56$ MHz. Because of the different mobilities of ions and electrons only the latter can be accelerated in the oscillating fringe regions of the plasma to ionize atoms. Due to this and the conductivity of the plasma the electric field "self-biases" between the cathode and the plasma edge. Since the electrons are repelled by the cathode a room charge of positively charged ions is created near the target [63].

Sputtering allows for rather high deposition rates when compared to other methods like evaporation. Because of the reduced deposition time, it is possible to work with comparably high background pressures (usually $10^{-7}$ to $10^{-6}$ mbar) and still get good results. The sputtering rate is influenced by the distance between target and substrate, the applied voltage, and to a lesser degree by the sputtering gas pressure. The sputtering rate is approximately inverse proportional to the distance and - above the plasma ignition threshold value - proportional to the voltage. With these parameters fixed, the thickness of a deposited film can be determined with the time of deposition and the film thickness-derived sputtering rate of a previously measured reference sample.

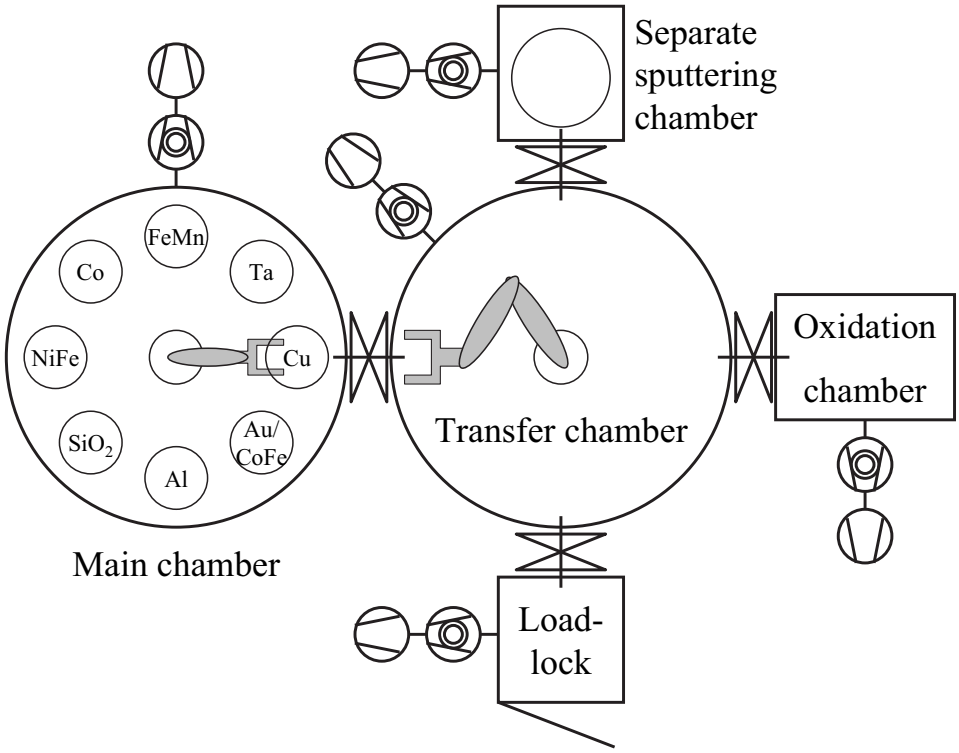


Figure 2.2: *Schematic top view of UNIVEX 450 B sputtering system.*

The deposition system used for this work is a Leybold UNIVEX 450B sputtering tool, installed in 2000. Its general lay-out is depicted in Fig. 2.2. In its main chamber there are eight cathodes with interchangeable 4" targets. One of the cathodes is connected to an RF generator, the others are DC sources. A programmable turn-table capable of handling 4" substrates is mounted below the targets with a target-substrate distance of 6 cm. It is possible to rotate the turn-table during desposition which leads to an effectively lowered deposition rate as the substrate is positioned below the target for a shorter time only. The background pressure of the main chamber is around $5 \cdot 10^{-7}$ mbar, sputtering gas pressure ranged from some $10^{-3}$ to some $10^{-2}$ mbar. Possible process gasses are Ar, $N_2$, and $O_2$, although in this work only non-reactive sputtering with Ar was used. All targets were always subjected to a pre-sputtering cleaning process before actual deposition

took place. A list of materials and their usual sputtering parameters is shown in table 2.1. The sputtering rates in this table were usually measured with a DEKTAK profiler or by X-ray reflection measurements. For profile measurements, a material was deposited for a certain amount of time on a substrate with felt-tip pen markings on top. The markings were removed in an acetone bath, taking along the deposited material on top of them. The created edges allowed height difference measurements with the needle-based profiler. With this difference and the deposition time the sputtering rate could be calculated.

| Material | Position | Power $[W/cm^2]$ | Ar-Pressure [mbar] | Rotation | Sputtering rate [nm/sec] |
|---|---|---|---|---|---|
| $SiO_2$ | 1 | 7.6 | $1.2 \cdot 10^{-2}$ | no | 0.67 |
| $Ni_{21}Fe_{79}$[1] | 2 | 1.9 | $6 \cdot 10^{-3}$ | no | 0.81 |
| Co | 3 | 1.9 | $6 \cdot 10^{-3}$ | no | 0.64 |
| $Fe_{50}Mn_{50}$ | 4 | 1.9 | $6 \cdot 10^{-3}$ | no | 0.69 |
| Ta | 5 | 1.9 | $6 \cdot 10^{-3}$ | no | 0.90 |
| Cu | 6 | 1.3 | $6 \cdot 10^{-3}$ | no | 1.13 |
| $Co_{75}Fe_{25}$ | 7 | 1.9 | $6 \cdot 10^{-3}$ | no | 0.77 |
| Au | 7 | 1.3 | $6 \cdot 10^{-3}$ | no | 1.70 |
| Al | 8 | 1.9 | $6 \cdot 10^{-3}$ | yes | 0.045 |

Table 2.1: *Sputtering materials in UNIVEX 450B*

The UNIVEX 450B system has a second, separate sputtering chamber with a 6" target which was not used for this work. The chamber is used for materials which are not to be contaminated with ferromagnetic materials. Another chamber is reserved for the oxidation process which is detailed in

[1]This is not to be confused with permalloy ($Ni_{79}Fe_{21}$) which was intended as material. A wrong order switched the composition ratios of the alloy and this mistake was not discovered until most of the samples and measurements were finished. More in chapter 4.1

chapter 2.2.

The sputtering system is programmed via an SPS system (Co. Siemens) so that multi-layer deposition, oxidation steps, and transfers between chambers are executed automatically.

## 2.2 Oxidation processes

The tunneling junctions fabricated for this work always used aluminium-oxide ($AlO_x$) as tunneling barrier. The fabrication of this oxide was achieved by first depositing 1.3 nm of metallic aluminium and subsequently oxidizing the metal as experience shows that this process does by far not lead to as many pinholes as depositing insulating $AlO_x$ directly. Since the barrier resistivity is exponentially dependent on its thickness, the biggest part of current will flow through the thinnest parts ("hot spots") of a rough barrier. Since this will lead to higher thermal stress in these hot spots a break-down of the barrier becomes more likely which makes it necessary to produce barriers as smooth as possible.

Further, different oxidation processes yield varying stoichiometry and amounts of impurities in the barrier which influence the tunneling properties, especially the spin conservation [45]. The parameters of the oxidation process must also be tuned so that there is neither over- nor under-oxidation. If there is an amount of unoxidized Al left at the interface of the ferromagnetic electrode and the barrier, the paramagnetic Aluminium will lead to an increase in spin-flip and a decrease of the TMR value of the magnetic tunneling junction [64]. If the oxidation process also affects the ferromagnetic electrode which in this work usually contained Co, various Co-oxides are formed. Some of these exhibit antiferromagnetic behavior which also leads to a strongly reduced spin conservation and thus a reduced TMR value [65].

## Oxidation mechanism

For the oxidation of aluminium various methods have been proposed and used. To understand the aims of these methods a basic understanding of the oxidation process is necessary. Cabrera and Mott gave a comprehensive report in [66].

The oxidation of aluminium in a pure oxygen atmosphere can be studied most easily as was most recently done by Martin [67] and Chen [68]. The first monolayer of an aluminium layer oxidizes very fast even in high vacuum due to the remaining oxygen in the residual gas pressure. A background pressure of $10^{-6}$ mbar the uppermost monolayer is covered with the residual gas in 1 sec [63] which in the case of oxygen also means the oxidation of the aluminium monolayer. If further oxygen is present which adsorbs on the oxide surface, a tunneling process of electrons is possible. The Fermi energy in aluminium is higher than the energy of the lowest unoccupied orbital of an oxygen atom. Therefore conduction electrons can tunnel out of the metal to the oxide-gas interface. This leads to the formation of an electrical field across the oxide. As long as this field is strong enough (i.e. the barrier is not too thick) positively charged Al ions are moved through the barrier where they become oxidized by the present oxygen. This process is limited by the electric field which is given by the potential difference between the Fermi level in Aluminium and the energy level of the lowest unoccupied oxygen orbital. Therefore this process is self-limiting to a certain thickness. A further limiting factor is the fact that the ion movement across the oxide is hindered by the metal-oxide interface potential and between favored lattice positions. This can be influenced by thermal activation or application of an additional electric field across the barrier. Results of the influence of thermal activation are also shown in [67].

The pure oxygen process leads to aluminium-oxide barriers with resistance-areas products of several $\Omega\mu\mathrm{m}^2$ [69, 70].

Oxidation in ambient air differs from oxidation in pure oxygen mainly through the presence of water in the atmosphere. Among other reaction prod-

ucts aluminium-hydroxide is formed [71]. Nevertheless the group of Miyazaki reported magnetic tunneling junctions which were fabricated with ambient air oxidation and showed TMR values of over 15% at room temperature [4].

## Anodization and plasma oxidation

As mentioned above an imposed or additional electric field across the barrier during oxidation can increase the oxide thickness and thus the resistance-area product. This can be achieved by so-called anodization where the voltage is applied between the metal as anode and the oxygen. The contact to the latter is made by a liquid electrolyte or through a plasma. Both provide the oxygen for the oxidation. Liquid electrolyte anodization is known from superconducting Josephson junctions where an oxygen-rich electrolyte, ammonium pentaborate, is used to oxidize either Aluminium or Niobium [72]. This method is disadvantageous however, since it is necessarily ex-situ and so impurities can collect on top of the aluminium before and after anodization.

The other anodization method employs an in-situ oxygen plasma and is commonly referred to as "plasma oxidation". After deposition of the Aluminium layer an oxygen plasma is ignited. In the plasma the oxygen molecules are dissociated to $O^-$-ions and free radicals. Especially the latter increase the oxidation rate and the oxidation time is reduced to a few minutes or even seconds. Much thicker oxide layers are possible, although it is difficult to achieve CMOS-compatible low resistance-area products. Plasma oxidation was first used for Josephson junctions in [73] and has become fairly usual for the oxidation of the barrier in magnetic tunneling junctions. In [74] junctions with $RA$-products of several 100 $\mathrm{k}\Omega\mu\mathrm{m}^2$ are shown, although newer results with samples which use Al-layer thicknesses of around 7 Å show $R \cdot A$ products of slightly less than 1 $\mathrm{k}\Omega\mu\mathrm{m}^2$ [75].

## UV-light assisted oxidation

The oxidation process for tunneling barriers in this work used another method to enhance the oxide thickness. The aluminium was oxidized in-situ with pure oxygen while an ultraviolet (UV) lamp was present and illuminating the sample. This method was reported by Cabrera [76] and was used for superconducting Josephson junctions by Fritzsch [77]. The UV-light assisted oxidation of tunneling barriers for magnetic tunneling junctions was first developed by Rottländer [78, 79, 80], further results are found in [81, 82].

In the UNIVEX 450B sputtering system a 23 W power low pressure mercury lamp was present in the oxidation chamber. It was positioned above the substrate holder in the focal axis of an aluminium paraboloid mirror which focussed the light of the lamp parallel onto the substrate plane. The main UV lines of the mercury lamp are at 254 nm and 185 nm where the latter is ten times weaker than the first. The aluminium mirror reflects the 185 nm line with more than 90%.

The influence of the UV light on the oxidation process is twofold: On one hand ozone is generated. The 185 nm line is able to dissociate $O_2$ into atomic oxygen which in turn reacts with $O_2$ to ozone ($O_3$). Both mercury main UV lines are also able to dissociate ozone again.

On the other hand the photoelectric effect of the UV light photons on the oxidation process (again described by Cabrera-Mott [66]) has to be taken into account. Although the photons from both lines can be absorbed as described above, even at an oxygen atmosphere of 100 mbar the absorption length of the 185 nm line is about 30 cm and that of the 254 nm line even longer. With a distance of UV lamp and substrate plane of 5 to 10 cm clearly a majority of photons reaches the sample surface. Photons absorbed in the metal excite metal electrons which increases the amount of electrons tunneling through the formed oxide and increasing the surface charge at oxygen sites. This increases the electric field across the oxide and leads to a higher possible oxide thickness.

The maximal potential increase through the UV light can be derived by

the photon energy $U_{max} = h\nu/e$. This means that the oxide thickness is proportional to the used photon energies.

## 2.3 Lithographic patterning

For transport measurements a deposited tunneling multi-layer has to be structured laterally. The lateral size for junction areas used in this work varied usually from slightly below 1 to 100 $\mu$m. Shadow mask technologies which utilize masks on top of substrates during deposition don't allow small enough feature sizes. Therefore, optical lithography and ion beam etching was employed.

In the process of lithography, the multi-layer is covered with a UV-light sensitive lacquer, the "photo-resist" (in this work from Hoechst Co., AZ 5214E). With the help of a chromium-patterned glass mask the photo-resist is exposed to UV-light (main wavelength $\lambda = 320$ nm), thus transferring the chromium-pattern onto the lacquer. The substrate is put into a bath of developer (Hoechst Co., MIF 326) that dissolves the exposed parts of the lacquer much faster than the unaffected parts.

These exposed parts can be removed with an etching process. Since the resist is much thicker ($\approx 1.4$ $\mu$m) than the usual multi-layers even non-selective etching methods will affect only the free parts on the substrate while leaving enough resist on top of the places which are not to be removed. After the etching the resist can be removed in a solvent bath (i.e. acetone or n-methylpyrillidon).

The etching process can be either chemical or physical. In either case two criterions have to be met: It must be possible to stop the etching precisely at one of the nanometer-thin layers and the resist pattern must be mapped to the substrate fairly accurately. Chemical etching is usually very selective and isotropic. This means that - given the correct chemistry - a defined etch-stop is possible but under-etch below the resist-protected areas is takes place (cf. Fig. 2.3a). Physical etching processes which were used in this

work are ion etching or ion beam etching. These techniques use accelerated ions usually generated in a plasma like in sputtering processes. The ions hit the substrate surface and dislocate atoms layer by layer. If an inert gas is used for the plasma generation (i.e. Ar) the process is purely physical and practically non-selective and anisotropic (cf. Fig. 2.3b). It reproduces the resist pattern rather well onto the substrate. Non-selectivity is given since the etching rate doesn't vary much with the materials used in this work.

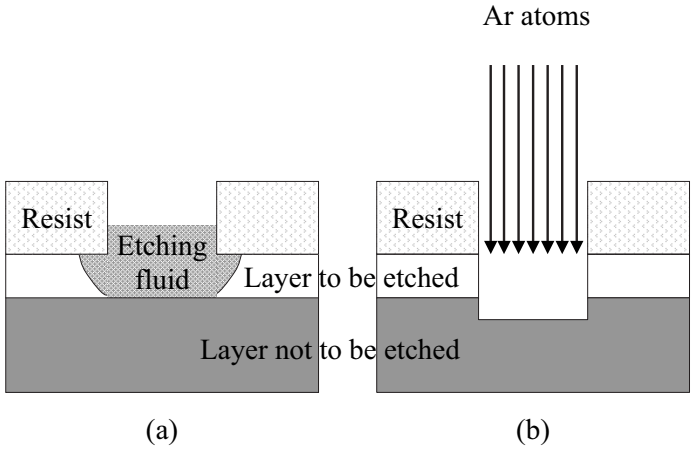


Figure 2.3: *Profiles of thin film etching: (a) chemical etching (b) physical ion etching.*

This limitation can be overcome by monitoring etched material with analytical tools, here mass spectroscopy. Quadrupole secondary ion mass spectrometers (SIMS) were present in two different ion beam etching tools (both from Oxford Co.) used for samples. They detect ions in dependence of their specific mass $m/e$. The persistence of etched material in the vacuum chamber is limited so that layer for layer can be detected. Fig. 2.4 shows an example of the etching of a complex layer structure. From top to bottom the layers were Au/NiFe/CoFe/$AlO_x$/CoFe/FeMn/NiFe/Cu/NiFe/Ta/$SiO_2$/Si-substrate. Except for Au which is not ionized during etching the graph in the figure shows each single layer as it is etched. Of note is the sensitivity of the mass spectrometer to Al which allows very accurate etch stops below

the $AlO_x$ barrier. More details on ion beam etching are found in [83].

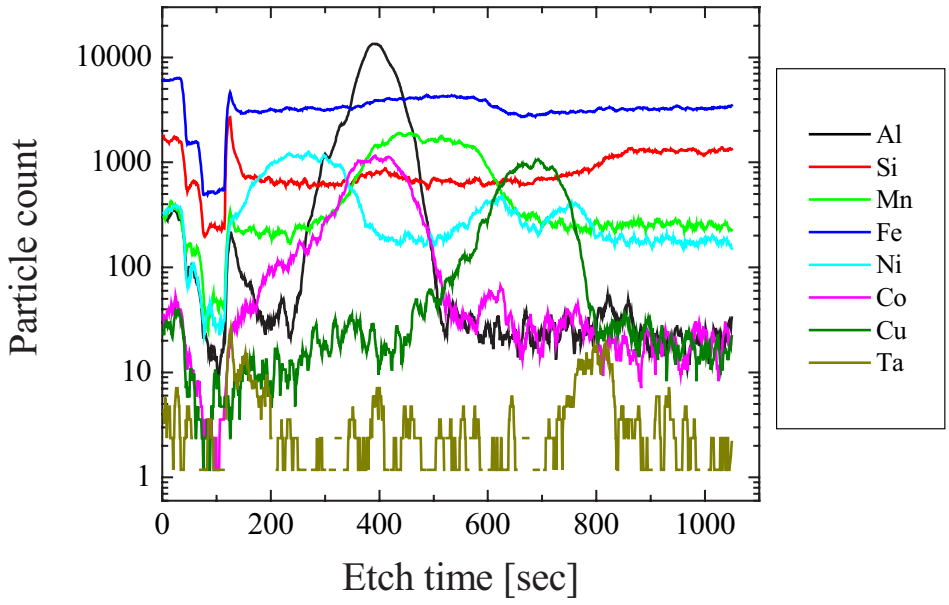


Figure 2.4: *Mass spectrometer graph: Particle count in dependence of etching time of Au/NiFe/CoFe/$AlO_x$/CoFe/FeMn/NiFe/Cu/NiFe/Ta/$SiO_2$/Si sample.*

Except for removing material to structure a sample laterally it is also possible to deposit new layers to achieve a certain functionality. For the samples in this work it was necessary to deposit an insulating material (e.g. $SiO_2$) after etching to electrically disconnect the bottom from the top electrodes. After this, with a new resist mask also a conducting top lead (e.g. Cu, Au) was deposited. In these cases, the whole wafer becomes covered in the new material. If the wafer then is put in a solvent like acetone, the photo resist with the new material on top is lifted and can be rinsed away. This process is called "lift-off". In practice a few steps have to be taken care of for lift-off. The lithography step described above is a so-called positive resist process since a positive picture of the glass/chromium mask is mapped to the resist. The developing rounds off the edges of the resist towards the coated areas (cf. Fig. 2.5a). For lift-off this is undesired as the solvent cannot reach

below the resist areas which are now covered by a new material. Therefore the so-called negative resist process is used. By heating the resist layer to 120 °C for some time after exposing through the mask the exposed areas are hardened. A subsequent complete exposure of the whole resist ("flood exposure") then allows the selective removal of the previously unexposed areas in a developer fluid. The edges of the resist in this process are slanted outwards which allows for an easier lift-off (cf. Fig. 2.5b). Table 2.2 recapitulates the lithography steps for the two different processes. The reproducible fea-

| | Positive Process | Negative Process |
|---|---|---|
| Spinning on of resist | 1.4 $\mu$m | 1.4 $\mu$m |
| Baking | 90 °C, 4 min | 90 °C, 4 min |
| Mask exposure | 20 sec | 20 sec |
| Hardening | | 120 °C, 45 sec |
| Flood exposure | | 60 sec |
| Developing | $\approx$ 120 sec | $\approx$ 40 sec |

Table 2.2: *Lithography processes*

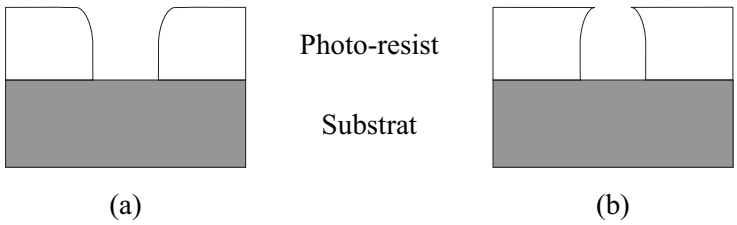


Figure 2.5: *Resist edges in different lithography processes: (a) positive process (b) negative process.*

ture size for both positive and negative processes was 1 $\mu$m. Slightly smaller feature sizes could be achieved for positive processes in single cases when the resist was kept in the developer for a longer than usual time. Through

this over-developing the unexposed resist was also removed from the sides leading to smaller structures. Although this method is not very controllable a great array of structures on the same wafer always showed enough desired feature sizes down to about 0.6 $\mu$m. The junction sizes in these cases had to be measured by (light-)microscopy and could not be derived from the mask junction sizes.

## 2.4 Multi-layer lay-out

A magnetic tunneling junction consists of three principal regions: a ferromagnetic bottom electrode, the tunneling barrier, and the ferromagnetic top electrode. The easiest approach therefore is to use layer compositions like $Co/Al_2O_3/Ni_{79}Fe_{21}$ [78, 84]. The hard-magnetic Co and the weak-magnetic $Ni_{79}Fe_{21}$ (permalloy, Py) have differing coercive fields so that they can be aligned easily parallel or antiparallel with an external magnetic field to measure their tunneling magneto resistance. But this tri-layer structure has several disadvantages:

- The TMR value is not very high due to the comparably low spin polarization of Co respectively Py.
- Usually the switching fields are not very far from each other so that antiparallel alignment is difficult to achieve.
- Using Co as bottom lead is not favorable since it has a high specific resistance and this can lead to current distribution effects in the electrode which falsify the TMR measurements [78].

The highest spin polarization in metallic alloys of Fe, Co, or Ni is reached in a range of $Co_{1-x}Fe_x$ alloys (as seen in table 1.1). By using $Co_{75}Fe_{25}$ for samples in this work for both electrodes a higher TMR value could be reached. For the TMR only the spin polarization at the metal-barrier interface is important so that the thickness of these layers could be kept very thin at 3 nm. To separate and stabilize the switching fields of the individual electrodes additional

layers were placed above and below. The top electrode CoFe was supposed to be covered with a thicker layer of 10 nm of weak magnetic Py. The direct contact of the metals leads to ferromagnetic coupling, the thinner CoFe layer follows the switching of the thicker Py layer. As said above, it was discovered that a wrong target was used for Py deposition and instead of $Ni_{79}Fe_{21}$ $Ni_{21}Fe_{79}$ was used. This material is not especially weak magnetic which explains some of the measured results discussed in chapter 4.4. The bottom electrode was pinned over the exchange-bias effect with an antiferromagnet (here: $Fe_{50}Mn_{50}$). A preferred alignment, or texture of the FeMn grains was necessary since only the $\gamma$-phase of $Fe_{50}Mn_{50}$ is antiferromagnetic [85]. $Fe_{50}Mn_{50}$ has a Néel temperature of $T_N = 520$ K and a Blocking temperature of around $T_B = 420$ K. The latter allowed aligning the uniaxial anisotropy of the antiferromagnet in the annealing steps performed on processed samples (see below). Loch showed that this texture is achieved when a seed layer (e.g. Ta) is placed on the substrate followed by a 3 nm thick Py texture layer [86]. Again, the use of a different NiFe alloy in this work explains shortcomings in the exchange-bias characteristics of fabricated samples. Nevertheless high resolution transmission electron microscopy (HRTEM) pictures of the structure of these layers show that (poly-)crystallinity is given after use of Ta as seed and $Ni_{21}Fe_{79}$ as texture layers (Fig. 3.3).

The last disadvantage named above, using a ferromagnetic high-resistive metal/alloy as bottom lead was addressed by incorporating a Cu lead above the Ta/NiFe texture layers. To keep the texture of the FeMn pinning layer, an additional NiFe layer was placed between Co and FeMn.

The complete stack was topped of by a cover layer to protect the uppermost NiFe layer from corrosion in ambient air. The cover material changed between Al, Cu, and Au. Thus the whole multi-layer lay-out usually was: Si-substrate, $SiO_2$, Ta(5), $Ni_{21}Fe_{79}$(3), Cu(20), $Ni_{21}Fe_{79}$(3), $Fe_{50}Mn_{50}$(20), $Co_{75}Fe_{25}$(3), Al(1.3) plus oxidation, $Co_{75}Fe_{25}$(3), $Ni_{21}Fe_{79}$(10), Au(5). The numbers in parentheses give the layer thickness in nm, Fig. 2.6 gives a schematic overview of the multi-layer structure.

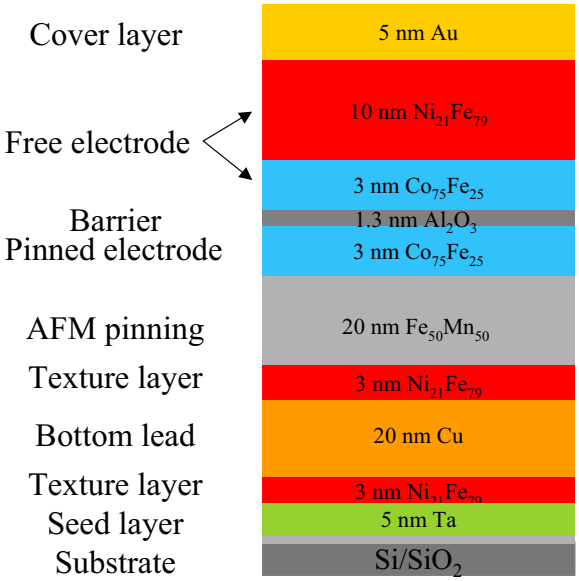


Figure 2.6: *Multi-layer lay-out for magnetic tunneling junctions.*

Fig. 2.7 describes the complete patterning process for the magnetic tunneling junctions.

In the first step a resist mask was placed on the substrate which defined the bottom lead. The complete stack was deposited on this mask followed by a lift-off process so that the stack remained in the form of the bottom-lead. A second resist mask was placed on the substrate which defined the junction shapes. In an ion-etching process the uncovered stack was removed down to the bottom lead. Now the same resist mask was kept and used to sputter deposit a usually 200 nm thick $SiO_2$ insulation layer. This insulated the bottom lead from the top lead which was deposited in the next step. Important for this insulation layer was the fact that sputtered $SiO_2$ is pin-hole free only from a thickness of 200 nm on [87]. After performing a lift-off process for the etching/insulating mask which uncovered the junction areas (and also the contact pad areas for the bottom lead) the last resist mask for the top lead was placed on the substrate. Through this mask the top lead of Al, Cu, or Au was deposited. The thickness of this wiring was usually

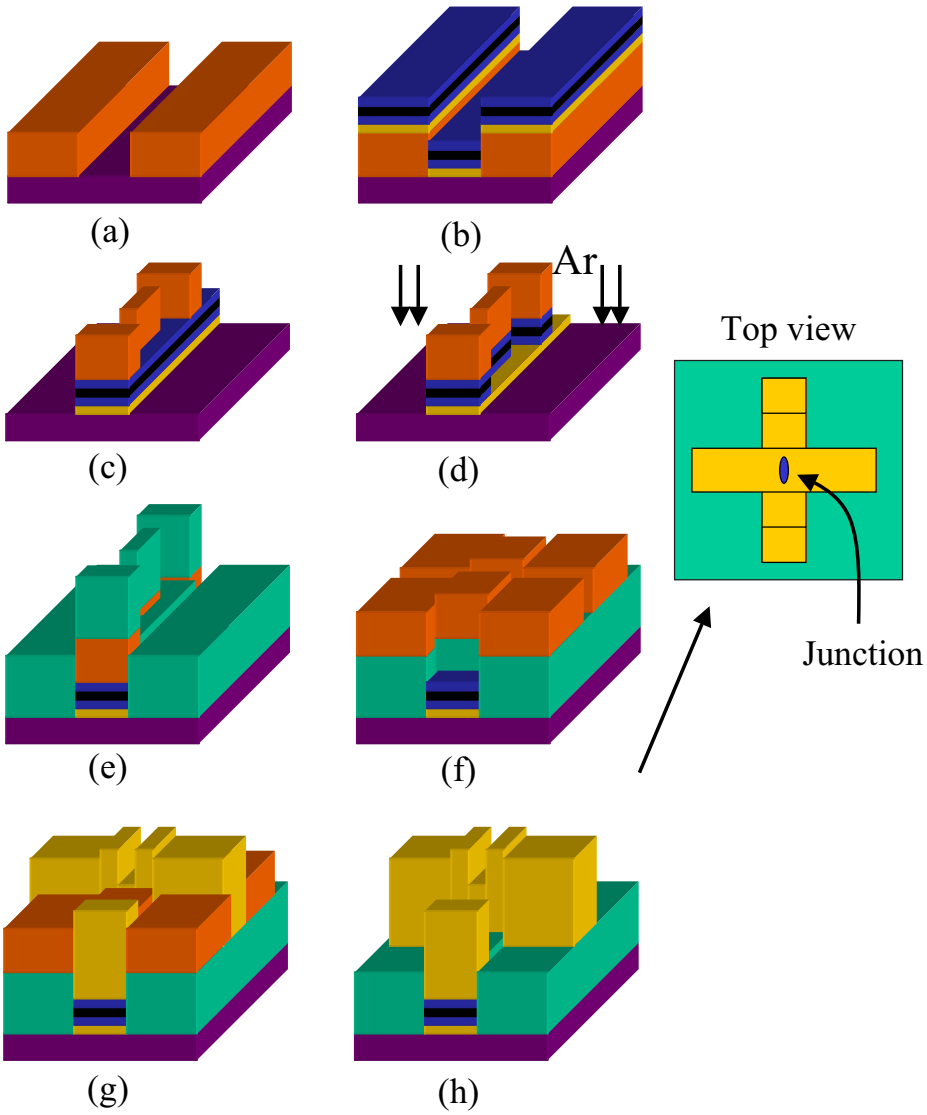


Figure 2.7: *Patterning of multi-layer for magnetic tunneling junctions: (a) resist mask for bottom lead (b) deposition of multi-layer (c) lift-off of resist and new resist mask for junctions (d) ion beam etching down to bottom lead (e) deposition of $SiO_2$ insulation (f) lift-off of resist and new resist mask for top lead (g) deposition of top lead (h) lift-off of resist.*

around 300 nm, always considerably thicker than the insulation layer so that there were no gaps in the lead at steps. After another lift-off process for this

mask the substrate was sawed into dices where necessary.

Usually substrates used were 4“-Si wafers which were covered by thermal $SiO_2$ and had a surface resistivity of more than 5 kΩcm. The lithography masks defined 1 cm × 1 cm dies on the wafer. These were identical except for several test dies which allowed to check individual process steps. On one die junctions were grouped in five columns with 15 rows of five junctions each. Each group of five junctions used the same bottom lead and individual top leads in cross geometry. Each of the 5 big rows grouped same junction geometries: Circles, ellipses, ship bows, squares, and rectangles. The junction sizes ranged from 0.2 to 180 $\mu m^2$.

Since the sputtering system present for this work used 4“-targets the deposition on 4“-wafers led to a radial thickness variation across the substrate area. DEKTAK measurements showed that the layer thickness was 30% smaller at the edge of the 4“-wafer. The influence of this inhomogeneity was mainly important for the aluminium layer thickness and the derived barrier thickness. This variation allowed to measure the thickness dependence of barrier resistance and TMR.

## 2.5 Sample annealing

Several characteristics of magnetic tunneling junctions can be influenced by annealing processes. Heating the substrate to a certain temperature after the patterning process is finished, keeping it at that temperature for some time, and cooling it again results in changes of the multi-layer. As temperature increases first the tunneling barrier is modified by re-ordering of the oxide sites which was observed by the group of Freitas with the help of Rutherford back scattering measurements [88]. At higher temperatures diffusion of metals between layers starts, for example at 250 °C Co starts to diffuse [89] and Mn at 300 °C [90]. Reaching a temperature of 350 °C diffusion into the $AlO_x$ barrier leads to the formation of pinholes.

If the cooling part of the process is conducted in a sufficiently high mag-

netic field it is possible to re-align the antiferromagnetic layer. The latter is only possible if the annealing temperature exceeds the Blocking temperature of the antiferromagnetic layer (cf. chapter 1.5).

The annealing in this work was conducted in two different fashions. One possibility was to heat a wafer inside the oxidation chamber inside the UNIVEX 450B sputtering system. It contains a heater for temperatures up to 350 °C. For thermal coupling between heater and sample an atmosphere of 10 mbar of inert gas (usually Ar) was inserted into the chamber. In the oxidation chamber a permanent magnet for aligning the antiferromagnet was present as well. It applied a magnetic field of 10.3 kA/m in the wafer plane with homogeneity of 2% in a 4“ radius.

The second possibility was ex-situ heating on a heater which could be placed inside an electromagnetic coil (whose characteristics are described in more detail in chapter 4.1). This allowed for heating up to 450 °C in variable fields up to 400 kA/m. Of course, this second method exposed the sample to ambient air oxygen and water during heating.

# Chapter 3

# Structural characterization

Structural characterization techniques were employed for deposited film stacks that were not patterned. These measurements allowed insights into roughness, film homogeneity, and magnetization characteristics.

## 3.1 Transmission electron microscopy

The characterisation of a sample with transmission electron microscopy (TEM) gives insights on thin film crystal structure and layer topology. To conduct TEM the sample substrate is cut into thin stripes, two stripes are glued to each other, and with polishing the sample is thinned down to a thickness of several micrometers. After this preparation an electron beam can penetrate the sample and its diffraction is measured. Subsequent analysis of the diffraction data can lead to lateral view images of a sample on nanometer scale, even allowing to see crystal axes. Details on TEM technology are found in [91], the TEM measurement in this work were conducted by Dr. C. Jia of the Institut für Mikrostrukturforschung, Forschungszentrum Jülich.

Fig. 3.1 gives a large scale overview of a MTJ stack of the composition Si-substrate, $SiO_2$, Ta(5), $Ni_{21}Fe_{79}$(3), Cu(20), $Ni_{21}Fe_{79}$(3), $Fe_{50}Mn_{50}$(20), $Co_{75}Fe_{25}$(3), Al(1.3) plus UV-light assisted oxidation, $Co_{75}Fe_{25}$(3), $Ni_{21}Fe_{79}$ (10), Au(5) (film thickness in nm). The TEM picture shows the $Al_2O_3$ layer

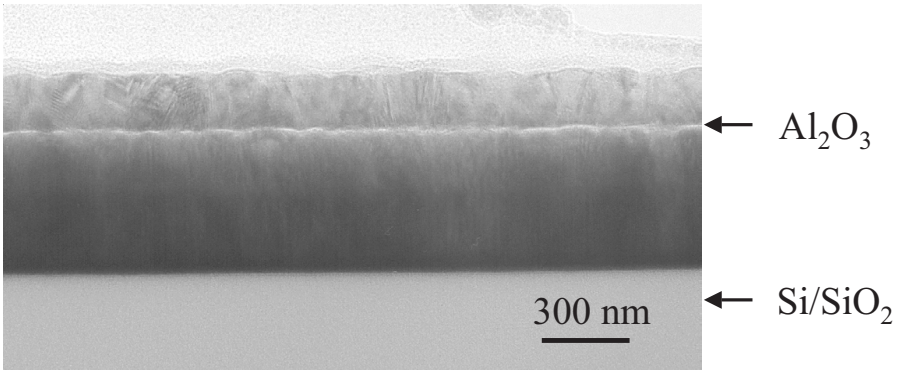


Figure 3.1: *TEM measurement of MTJ stack.*

as wavy but continuous line in the upper third. The other layers cannot be distinguished in this resolution. A high resolution TEM measurement of the region around the barrier is shown in Fig. 3.2.

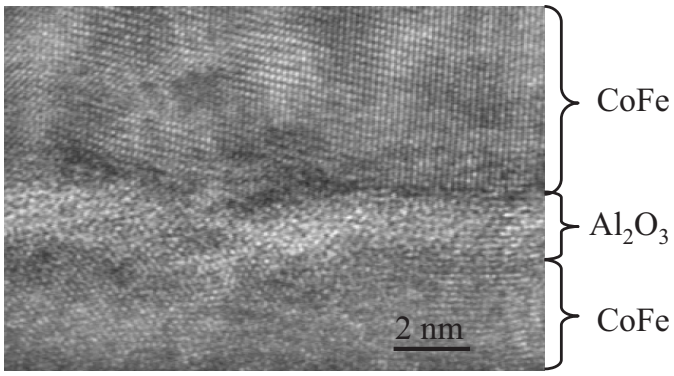


Figure 3.2: *High resolution TEM measurement of $Al_2O_3$ barrier region in MTJ stack.*

The top and bottom CoFe electrodes show a crystalline structure where the $Al_2O_3$ barrier is amorphous. The thickness of the barrier amounts to the expected 1.7 nm. From this measurement the roughness of the bottom stack even on this small scale is visible by the waviness of the barrier. Nevertheless the barrier appears to be pinhole-free.

A high resolution measurement of the seed and texture layers (Fig. 3.3) gives insight on the texture formation. On top of the Si substrate the thin

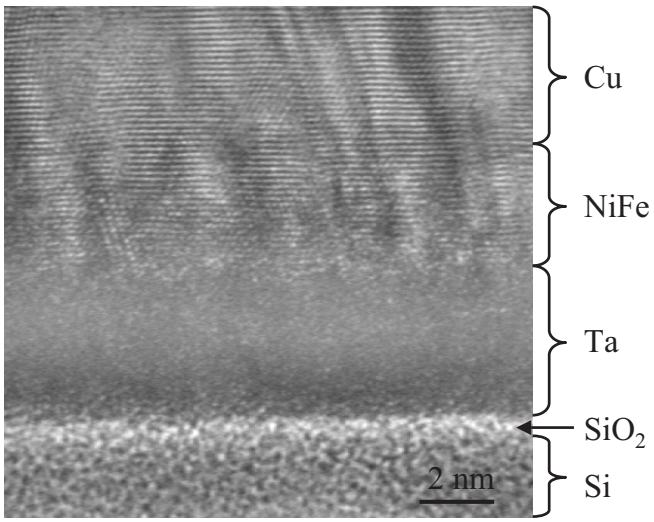


Figure 3.3: *High resolution TEM measurement of seed and texture layers region in MTJ stack.*

bright $SiO_2$ surface is visible. The Ta seed layer deposited on top of this appears amorphous but serves as seed for the structure of the layers on top of it. The first NiFe layer as well as the subsequent Cu layer show the crystalline structure which continues on to the CoFe electrode of the previous picture.

## 3.2 Scanning tunnel microscopy

Scanning tunnel microscopy (STM) is a raster probe microscopy method. It uses a conducting probe which is moved across the likewise conducting surface of a sample at a fixed distance which usually is of the order of several Ångstrom. At this distance the tunneling current between probe and sample is measurably high and by measuring it the distance can be calculated which results in a picture of the sample surface topography. The STM measurements were conducted at the Tohoku University in Sendai, Japan in the group of Prof. Miyazaki. The equipment was a sputtering system comparable in function to the UNIVEX system used for most of the samples

in this work. The Miyazaki sputtering system was connected to an UHV-STM chamber (Omicron Co.) where substrates with deposited films could be analyzed in-situ. The background pressure in the sputtering and oxidation chambers was $10^{-8}$ mbar and $10^{-9}$ mbar in the STM chamber. The time between deposition and measurement was in the range of 1 to 2 hours. Other details on the system and on specifics of the used system can be found in [92].

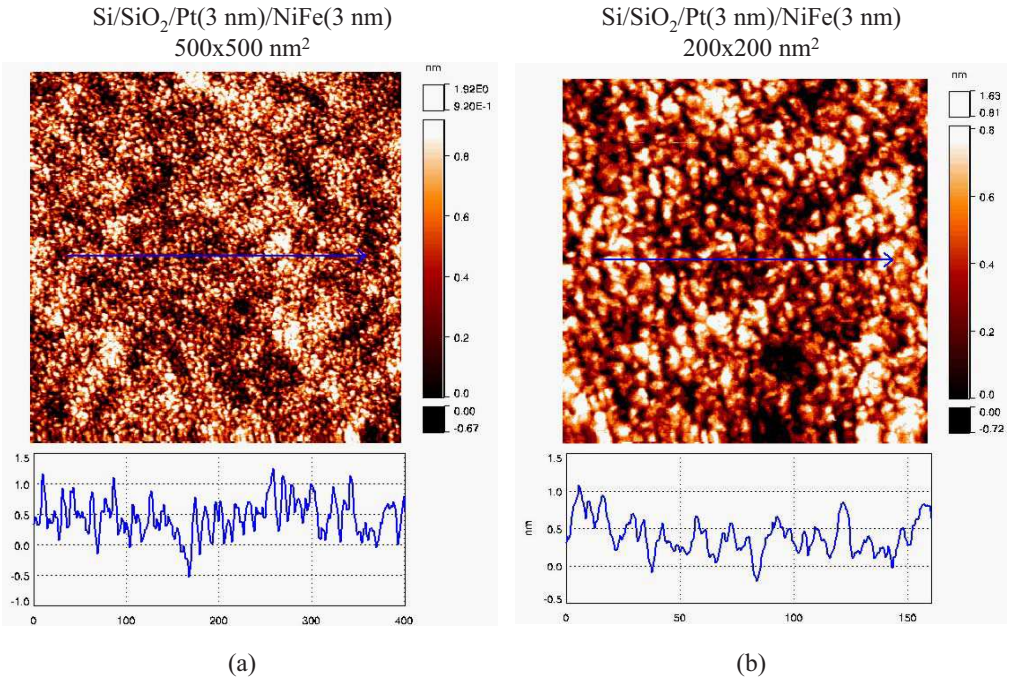


Figure 3.4: *STM measurements of Si, $SiO_2$, Pt(3 nm), NiFe(3 nm) stack. Measured areas: (a) 500 × 500 $nm^2$, (a) 200 × 200 $nm^2$.*

The STM analysis was used to compare roughness values previously obtained in this group by AFM [84] and to confirm the wetting effect of Al on transition metals which was examined earlier in this group by XPS [60]. Si substrates with a natural $SiO_2$ oxide surface were covered with model systems of the bottom electrode used through this work. Instead of Ta as seed layer, Pt was used in the STM samples which does not change the texture properties [93]. For each measurement the complete film stack was deposited anew

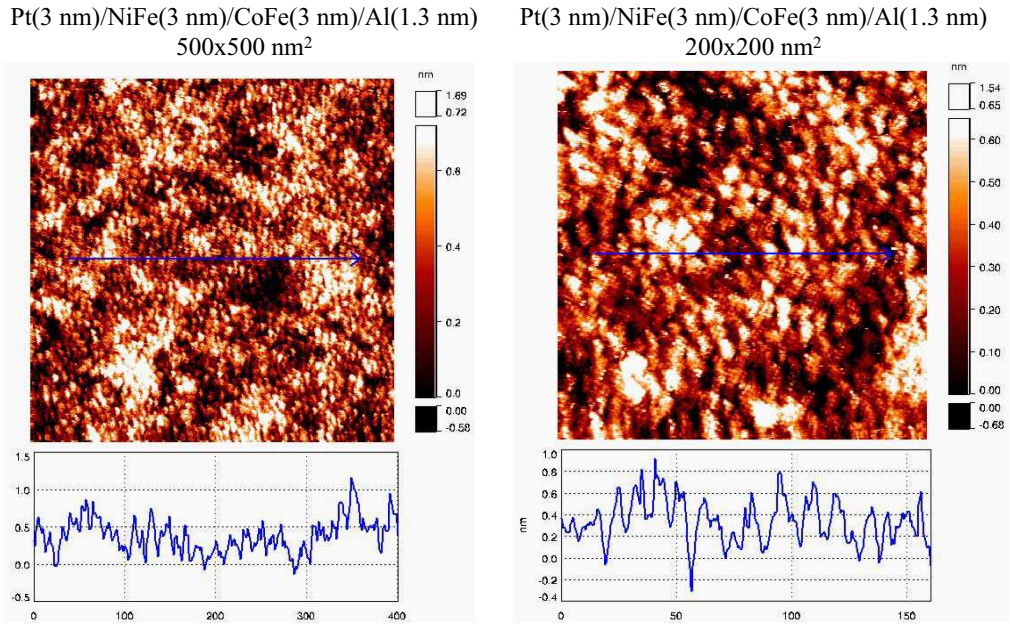


Figure 3.5: *STM measurements of Si, $SiO_2$, Pt(3 nm), NiFe(3 nm), CoFe(3 nm), Al(1.3 nm) stack. Measured areas: (c) 500 × 500 $nm^2$, (d) 200 × 200 $nm^2$.*

to minimize contaminations which could appear during the time transfers and measurements took.

Fig. 3.4 shows the surface of a film stack comprised of Pt(3 nm), NiFe(3 nm). This represents the conditions of the stack near the substrate. The root mean square (RMS) roughness is 0.31 nm for the 500 nm measurement, respectively 0.27 nm for the 200 nm measurement.

This decreases after the film stack includes the bottom electrode CoFe and the (yet not oxidized) Al barrier (cf. Fig. 3.5. Here, the rms roughness is at 0.24 nm (500 nm measurement) respectively 0.22 nm (200 nm measurement). This confirms that Al films on transition metals like Co and Nb actually reduce the overall roughness of a film stack.

The subsequent oxidation of the Al film which was conducted by a plasma

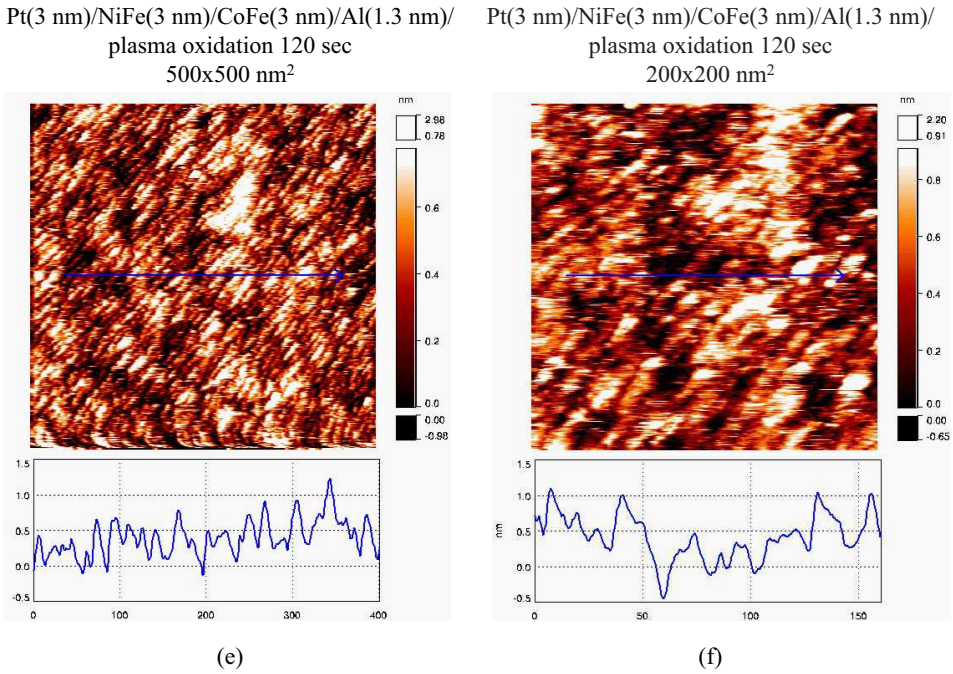


(e) (f)

Figure 3.6: *STM measurements of Si, $SiO_2$, Pt(3 nm), NiFe(3 nm), CoFe(3 nm), Al(1.3 nm), plasma oxidation (120 sec stack. Measured areas: (e) $500 \times 500\ nm^2$, (f) $200 \times 200\ nm^2$.*

oxidation process slightly increases the rms roughness again (cf. Fig. 3.6)[1]. An overview over all roughness values can be found in table 3.1. Since the roughness of the complete stacks stays well below the thickness of the aluminium oxide (nominally about 1.7 nm) a pinhole-free tunneling barrier is feasible under these conditions.

[1]It has to be noted though, that the measured higher roughness values in this last case can derive from a measurement artefact. Since the oxidation leads to a significantly higher resistance the measured currents decrease by several orders of magnitude. Therefore the signal-noise ratio gets worse which can be observed in the measured pictures

| Stack composition | Measurement area [nm$^2$] | rms roughness [nm] |
|---|---|---|
| Pt, NiFe | $500 \times 500$ | 0.31 |
| | $200 \times 200$ | 0.27 |
| Pt, NiFe, CoFe, Al | $500 \times 500$ | 0.24 |
| | $200 \times 200$ | 0.22 |
| Pt, NiFe, CoFe, Al, oxid. | $500 \times 500$ | 0.26 |
| | $200 \times 200$ | 0.31 |

Table 3.1: *Rms roughness of film stacks as determined by STM measurements (see text for details on film thickness).*

## 3.3 SQUID magnetometry

With the help of SQUID magnetometry the magnetization hysteresis of (unpatterned) samples could be determined.

SQUID magnetometry uses a combination of superconducting materials and Josephson junctions to measure magnetizations with very high resolution. The central element of a superconducting quantum interference device (SQUID) is a ring of superconducting material with one or more weak links. Weak links are points in a superconducting ring with reduced critical current $j_c$. Through this the current density in the complete ring is very small which in turn leads to a small momentum of Cooper pairs in the whole ring. Thus the wavelength of the Cooper pairs is very long and there is little phase difference inside the SQUID. If a measuring current is passing through the SQUID which is slightly higher than $j_c$ a small voltage is measurable across the SQUID (while at the same time the AC Josephson effect causes an emission of electromagnetic waves with the Josephson frequency).

In a DC SQUID two Josephson junctions lie opposite to each other and in each in series to a resistance which reduces hysteresis effects. If magnetic field penetrates the interior of the SQUID the wave length of Cooper pairs changes depending on their direction of circulation in the SQUID ring. This leads to a phase difference and with increasing magnetic field this results

in a periodically changing voltage drop between the junctions. A detailed overview on SQUID principles and application can be found in [94].

A Quantum Design Co. MPMS2 SQUID magnetometer with applicable magnetic fields of ±46000 kA/m and temperatures from 1.8 to 400 K was used in this work. Measured samples were not patterned as the magnetization of structured thin films would have been too low to detect. Therefore the magnetization curves presented here are only qualitative in nature as structured samples would have much higher coercive fields due to form anisotropy. Measurements were conducted at low temperatures to increase signal gain and to reduce noise. This also does not change the qualitative behavior of the examined systems.

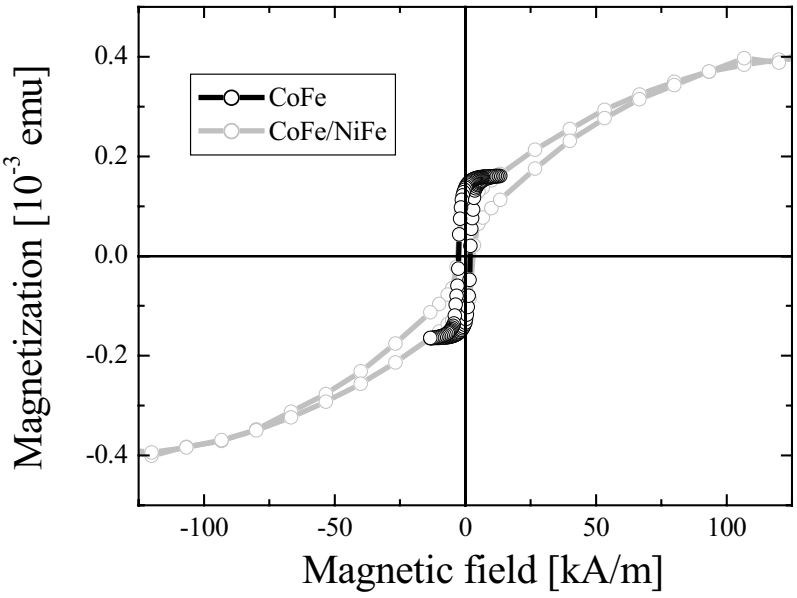


Figure 3.7: *Magnetization hysteresis loop measured via SQUID magnetometry of CoFe(4 nm) layer (black line) and CoFe(4 nm)/NiFe(10 nm) stack (red line). Sample size:* $3 \times 10$ *mm*$^2$*, measurement temperature* $T = 30$ *K.*

Fig. 3.7 shows the magnetization of the composite CoFe/NiFe top electrode compared to a single CoFe layer. It is visible that the hysteresis of the hard magnetic CoFe is modified by ferromagnetic coupling with the NiFe

layer. However, the coercive fields remain largely unchanged, which can be attributed to the fact that the $Ni_{21}Fe_{79}$ layer is not specially weak magnetic as would be expected from Permalloy.

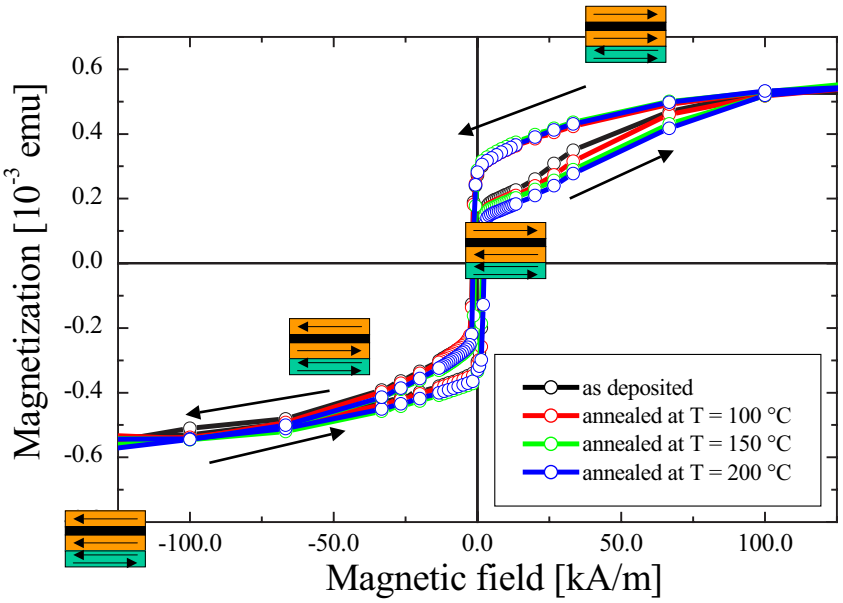


Figure 3.8: *Magnetization hysteresis loop measured via SQUID magnetometry of magnetic tunneling junction stack of composition as shown in 2.6. Measured as deposited and after consecutive annealing steps. Annealing was performed for 10 min in $N_2$ environment, cool-down in field of 87 kA/m. Sample size: $3 \times 10$ mm$^2$, measurement temperature $T = 30$ K.*

Fig. 3.8 shows the magnetization loops of a complete magnetic tunneling junction stack. The characterization was performed after subsequent annealing steps. Visible in all curves are the different magnetization switches of the free and pinned magnetization layers. This is overlayed with the magnetization curves of the NiFe texture layers which does not change the results qualitatively. The top layer switches sharply at a field value of $-16$ resp. 18 kA/m whereas the pinned layer shows a gradual switching behavior. For the switching field values the points where the hysteresis loop closes are taken which results in values of 65 resp. 110 kA/m. The exchange-bias caused uni-

axial asymmetry is seen in the difference between these two values. From the magnetization loops no change in these values after the annealing steps is derivable. However, the annealing does affect the magnetization of the pinned layer: With increasing annealing temperature the amount of pinned CoFe of the bottom layer increases, by an amount of $4.0 \cdot 10^{-5}$ emu which is 10 % of the complete difference of magnetization levels of the CoFe layer as seen in 3.7.

# Chapter 4

# Transport characterization

## 4.1 Measurement set-up

Transport measurements of structured samples were conducted in a four-point measurement set-up (see Fig. 4.1). This way, the influence of the lead resistances was removed from the measurement. A voltage controlled current source (VCS) supplied the current which passed through the tunneling junction. It was controlled by two voltage inputs. One is a voltage line ($\pm 10$ V) connected to a D/A converter and on to a personal computer. The second input is connected to a Hewlett Packard HP8904A function generator. With the function generator it was possible to apply an AC current to the junction for lock-in amplifier measurements. The two VCS inputs are added internally. The conversion ratio of the VCS is from $10^{-6}$ to $10^{-1}$ A/V allowing stable currents from about $10^{-8}$ to several $10^{-1}$ A.

The other leads of the cross geometry to the junction were connected to a preamplifier (either a Stanford Research SR560 model or an amplifier also built by the ISG electronic workshop). The preamplifier output could be measured by the personal computer through an A/D converter directly for current-voltage characteristics. For dynamic conductivity measurements a lock-in amplifier (Stanford Research SR530) was connected to the preamplifier. The reference AC voltage (usually 0.1 V, 140 Hz) which was

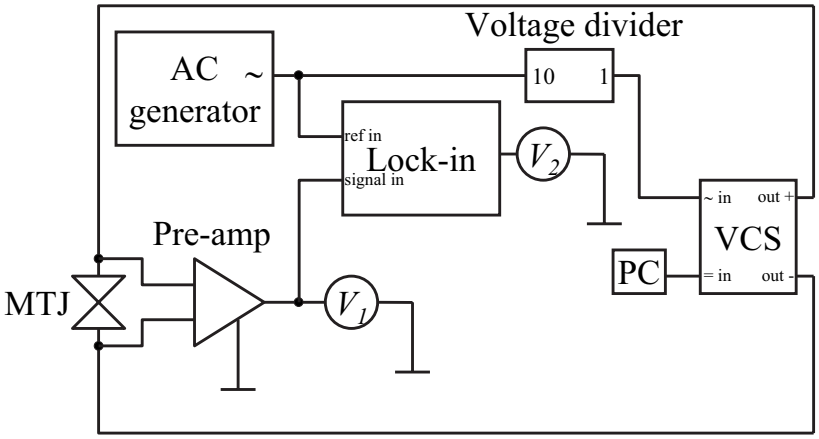


Figure 4.1: *Circuit schematic for MTJ fourpoint measurements. Pre-amp: Preamplifier; AC generator: Function generator; Lock-in: Lock-in amplifier;* $V_1$, $V_2$*: volt meters; PC: personal computer controlled voltage line; VCS: voltage controlled current source. The VCS' both inputs are added internally and a proportional current is supplied at the outputs.*

applied to the VCS also was used for the lock-in amplifier. The connection to the VCS was made over a 10:1 voltage divider decreasing the amplitude over which the lock-in measurement was averaged by a factor 10. The lock-in output also was recorded by a personal computer through an A/D converter.

The sample substrates were glued to carrier chips and connected to leads with Aluminium wires (diameter: 25 $\mu$m) that were bonded with an ultrasonic bonder (model Wedge 4523, Kulicke Co). The carrier chips themselves were mounted on IC sockets that were connected via twisted-pair cables to BNC connectors. With the BNC connectors it was possible to plug on the measuring tools and current sources.

Special care was taken to avoid unwanted electric breakthrough of the sample barriers. This occurs when higher voltages (more than about 1 V) are applied to the junctions. Since this can happen when plugging on or switching measurement devices as well as through static charge, short-cut bonds and potentiometers were placed between the leads.

Transport measurements were conducted with a flow cryostat capable of employing liquid helium (Spectrostat CF, controller ITC503, Oxford Co.). The temperature range of the cryostat is from room temperature down to 4.2 K and could be stabilized with an accuracy of 0.1 K. The cryostat itself was placed inside an electromagnetic solenoid (Bruker Co.). The solenoid had a bidirectional power source which enabled magnetic fields from −400 to 400 kA/m. The field was recorded by a Hall sensor (Group3 Co. Tesla-meter) mounted between one of the solenoid surfaces and the cryostat. Fig. 4.2 shows a schematic measurement set-up.

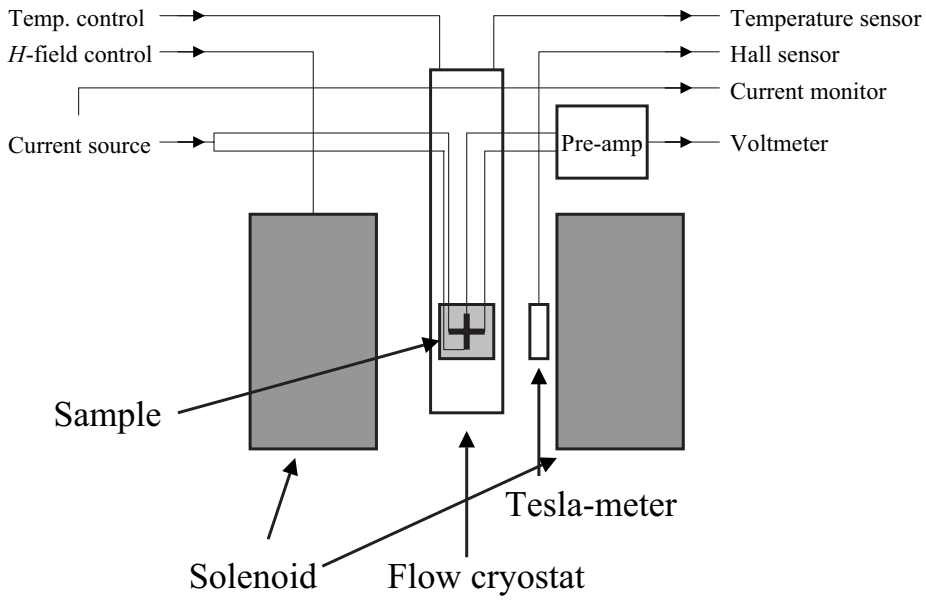


Figure 4.2: *Schematic flow cryostat and solenoid set-up for I-U and TMR measurements.*

Measurements were recorded and controlled by a PC. It was possible to regulate magnetic field, temperature, and junction current automatically. Simultaneously the feedback was recorded from the Tesla-meter, temperature sensors, current source monitors, and voltmeters. The necessary software for these operations was developed in this group [95].

Magnetic tunneling junctions were usually characterized in the following way: A current-voltage characteristic was taken by applying a set of current

values to the junction and recording the voltage drop across the sample. In the same manner conductivity-voltage measurements were made by using the lock-in amplifier output. Both measurements were also taken at different temperatures from room temperature down to the temperature of liquid helium. For measuring the tunneling magneto resistance (TMR) the sample current was kept at a fixed value and the magnetic field was swept bidirectionally. By recording the field values and in dependence on this the voltage drop the TMR curve was measured. This was done at different temperatures for measuring the temperature dependence of the TMR and also at different sample current values for seeing the bias dependence of the TMR.

## 4.2 On fitting

A lot of results on tunneling barriers in this work relies on deriving characteristics from Brinkman fits to the current-voltage characteristic. It has to be noted that the fitting equation presented in (1.10) is of a rather qualitative nature though. Fig. 4.3 shows a series of fit results. A current-voltage characteristic of a magnetic tunneling junction at room temperature (junction size 62 $\mu$m$^2$) was fitted by the Brinkman equation and the parameters $t$, $\varphi$, and $\Delta\varphi$ were derived. The voltage range for the fit was chosen differently as shown in the graph, from the negative value given to the positive value (e.g.: "50" represents a fit range from $-50$ to $+50$ mV).

The barrier parameters change continuously with different fit ranges. For higher voltages this is not surprising since the Brinkman fit explicitly is valid only for voltages below 10 % of the barrier height which is not fulfilled for values a lot higher than 100 mV. One can see that the thickness and height also linearly vary at smaller ranges without any obvious saturation. Thus the Brinkman fit depends on the fit range and its results are only of a qualitative nature. To be able to compare barrier parameters in this work the convention is to use Brinkman fits with a fit range of $\pm$100 mV unless noted otherwise.

Removing the central data range between $-20$ and 20 mV to eliminate

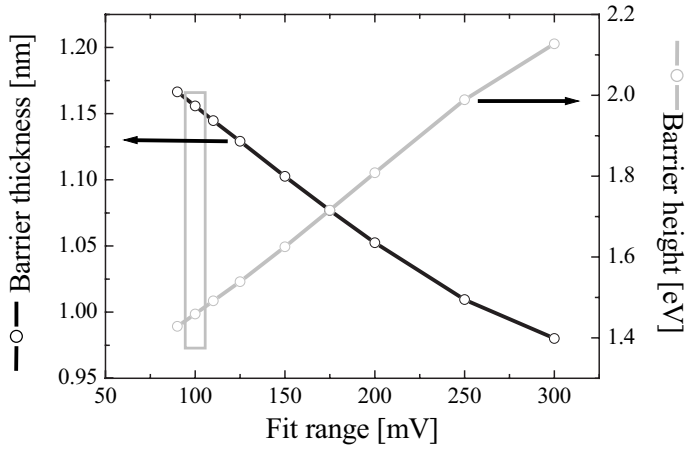


Figure 4.3: *Fitted barrier thickness and height in dependence of fitting range, sample # 1. Values on the $x$-axis indicate the absolute value of the negative to positive voltage range between which the fit was applied.*

the influence of zero-bias anomalies does not change fitting results in a meaningful way at room temperature. At low temperatures where the zero-bias anomaly peak grows (cf. Fig. 4.11b) important fitting will be adapted and the change in fitting range will be noted.

## 4.3 Barrier properties of magnetic tunneling junctions

A current-voltage measurement of a tunneling junction immediately yields the dynamic current characteristic $I(U)$. With the help of a Brinkman fit the barrier resistance $R$ (especially at $U = 0$) and the microscopic barrier properties thickness $t$, energetic height $\varphi$, and energetic asymmetry $\Delta\varphi$ are determined. With known junction area also the resistance area product $R \cdot A$ can be calculated. The calculated derivative $\mathrm{d}I(U)/\mathrm{d}U$ yields the dynamic conductivity characteristic $G(U)$. Towards this goal usually interpolation of the raw data was conducted to get equidistant data points. Also smoothing of either the $I(U)$ data or the derived $G(U)$ data was performed to reduce

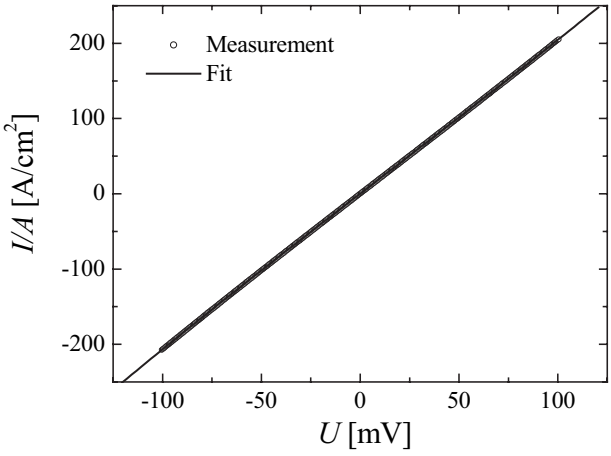


Figure 4.4: *Example of a current-voltage characteristic and Brinkman fit of sample # 1 at room temperature.*

noise.

Next to the calculated derivative $\mathrm{d}I(U)/\mathrm{d}U$ the dynamic conductivity could be measured with the help of the lock-in amplifier. The voltage output was proportional either to $R(U)$ when used in $1f$-mode or proportional to $\mathrm{d}R(U)/\mathrm{d}U$ when used in $2f$-mode. The noise of the resulting data was usually reduced by interpolation and smoothing. It was possible to calculate absolute resistance or conductance values from this data if an Ohmic reference resistor with comparable resistance was measured with the lock-in amplifier with the same settings. In this case it was possible to derive the junction resistance from the measurement directly.

Further current-voltage measurements conducted were for determining the temperature dependence of the tunneling barrier conductance. The sample was placed inside the flow cryostat and with the lock-in amplifier the resistance at usually zero bias was recorded while the temperature was decreased from 300 down to 4.2 K (or vice versa).

Magnetic tunneling junctions deposited and patterned like referred to in chapter 2.4 were first tested for tunneling behavior. A non-ohmic current-voltage characteristic was usually a first indicator for direct tunneling. But

only together with the temperature dependence of the conductance according to (1.25) and finally the presence of a high TMR value is the presence of a magnetic tunneling junction sufficiently proved. A high magneto resistance is needed to distinguish the field response from electrode AMR which has never been shown to be higher than about 1 % and which also exhibits peek values at the switching fields of the electrodes. Also, GMR values of aluminium-based systems was never higher than about 10 %.

In table 4.1 a list of those samples that appear in this work is listed with some of their properties. All further measurements were conducted with patterned samples of the layer structure shown in Fig. 2.6.

| # | Sample identification | Substrate size | Junction size [k$\Omega\mu$m$^2$] | Annealing state |
|---|---|---|---|---|
| 1 | Ff22 E2 II-14-3 | 4“ | 62.8 | as deposited |
| 2 | Ff24-1[1] | 4“ | varies | as deposited |
| 3 | Ff14 3-4-3 | $1 \times 1$ cm$^2$ | 35.3 | 10 min, 200 °C |
| 4 | Ff22 E-2 IV-15-3 | 4“ | 16 | as deposited |
| 5 | Ff19-1...4 | $1 \times 1$ cm$^2$ | 35.3, 16, 16, 4 | as deposited |
| 6 | Ff24-1 D-4 II-13-5 | 4“ | 141 | varies[2] |
| 7 | Ff24-1 C-4 V-15-4 | 4“ | 125 | varies[2] |
| 8 | Ff22 D-2 II-14-1 | 4“ | 15.7 | as deposited |
| 9 | IMEC[3] | 4“ | 12.5 | 10 min, 250 °C |

Table 4.1: *Magnetic tunneling junction samples appearing in this work.*

Fig. 4.4 shows the current-voltage characteristic of sample # 1 at room temperature. Using the Brinkman fit from eq. (1.10) on the I-U curve yields information on barrier thickness, height, and asymmetry. In this case the

[1]From this wafer several junctions were subjected to measurements. They appear together in an investigation on radial film thickness variations and are not indexed individually.

[2]See chapter 4.4.

[3]See chapter 4.6.

values gathered were $t = 1.16$ nm, $\varphi = 1.46$ eV, and $\Delta\varphi = 0.22$ eV. The junction resistance at zero bias is 786.0 Ω and the resistance-area product amounts to 49.4 k$\Omega\mu$m$^2$.

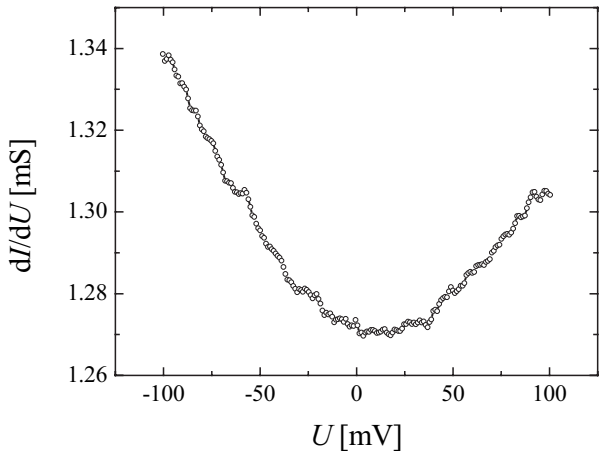


Figure 4.5: *Example of a conductance-voltage characteristic numerically derived from I-U graph from Fig. 4.4.*

A look at the numerically determined conductance-voltage derivative of the previous current-voltage characteristic gives a better look at the non-Ohmic behavior of the junction present, see Fig. 4.5. (expand)

It was mentioned that the deposition was not homogenous across a 4“-wafer. The resulting variations in layer thickness are most important for the Aluminium layer thickness as it influences the barrier resistance exponentially. Fig. 4.6 shows the resistance-area products of junctions across one wafer in dependence of the radial position of the junction. The $R \cdot A$ product decreases by a factor of 10 from the center of the wafer to the edge. The curve fitted to these data points shows that there is a general exponential dependence of the resistance to the radial position. The layer thickness seems to decrease roughly linearly with distance from the center. This is also pointed out by the barrier thickness as derived from Brinkman fits to the current-voltage characteristics of each data point (cf. Fig. 4.7. The thickness decreases from about 1.4 nm to 1.2 nm which is thicker than the nominal

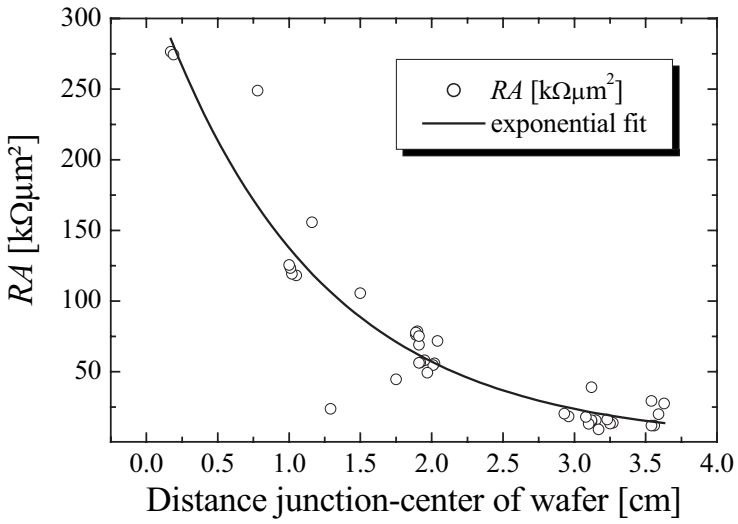


Figure 4.6: *Resistance-area products of junctions across sample # 2 in dependence of the radial position.*

$Al_2O_3$ thickness of 1.7 nm at the center and in accordance with the value at the edge (1.2 nm at a 30 % reduced deposition rate as determined by DEKTAK measurements). This allows the conclusion that the oxide in the center positions is rougher as the main part of the current seems to pass through areas of lesser thickness whereas the oxide at the edge is of less roughness. The smaller roughness at the edge can be derived directly from the fact that the layer thickness of *all* layers underneath is decreased by 30 %.

The barrier height of the measured junctions keeps in a range of 1.2 to 1.4 eV (cf. Fig. 4.8) indicating that the oxide quality is similar and mostly independent of the thickness. The deviating data points in Figs. 4.7, 4.8 result from junctions with local processing errors leading to a low-ohmic parallel conduction path or a high serial resistance on top of the top electrode. Both defects result in transport characteristics that can not be modelled with Brinkman fits and any attempt leads to abnormal values.

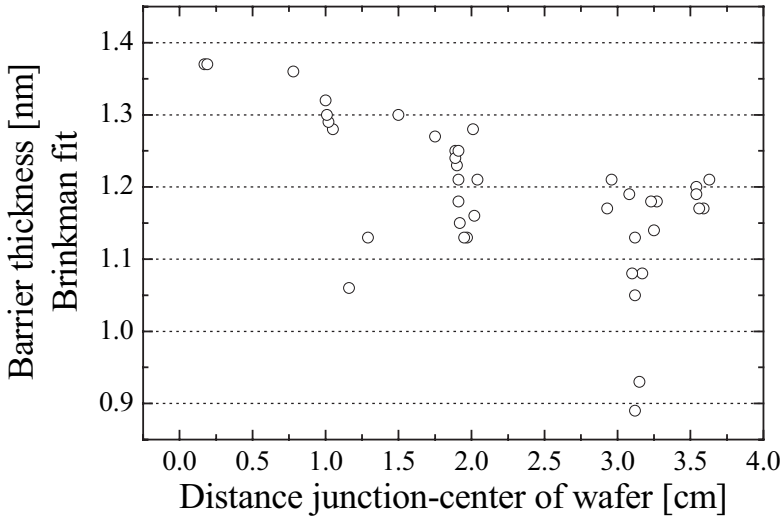


Figure 4.7: *Barrier thickness as derived from a Brinkman fit of junctions across sample # 2 in dependence of the radial position.*

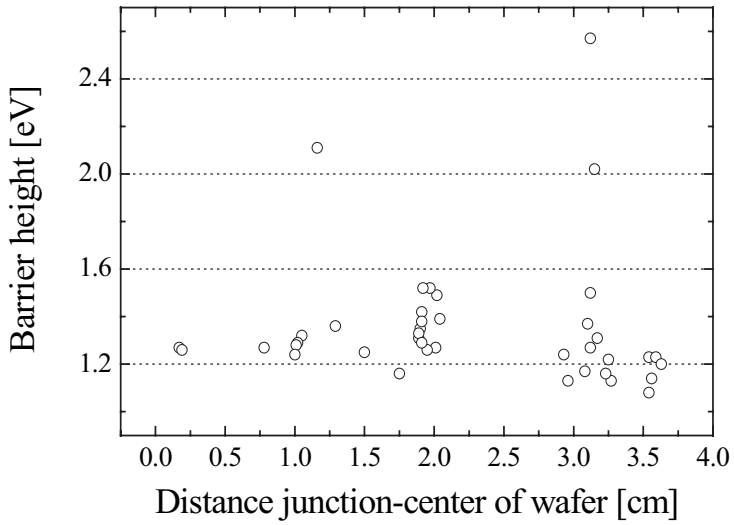


Figure 4.8: *Barrier height as derived from a Brinkman fit of junctions across sample # 2 in dependence of the radial position.*

The temperature dependence of the barrier conductance was investigated by two different approaches. On one hand current-voltage measurements were conducted at individual, fixed temperature values imposed on the sample inside the flow cryostat. The conductance value $G(T)$ was usually determined by applying a Brinkman fit to the measured values and taking the conductance from the derivative $\mathrm{d}I/\mathrm{d}U$ at $U = 0$ V of the fit at zero bias. This allowed for high temperature stability but only comparably few data points. The other approach used direct measurement of the relative conductance with the help of the lock-in amplifier and a continuous temperature change which was recorded with high data point frequency. For the temperature change the heater of the flow cryostat was set at a fixed value and the measurement was begun immediately after switching on the heater. Depending on the value of the heater power the temperature measurement of the sample was inaccurate. A too high gradient caused differences in the temperatures at the sample and temperature diode locations. Nevertheless this last method could give accurate results for the $G(T)$ dependence when the heater power was kept sufficiently small.

Measurements on $G(T)$ are found in section 4.4 since they also included the temperature dependence of the tunneling magneto resistance.

## 4.4 Tunneling magneto resistance

Magneto resistance measurements were conducted with the help of an external electromagnetic solenoid as described in chapter 4.1. The junction was mounted in the middle between the pole faces with the sample surface being in-plane with the magnetic field direction. A constant current was applied at a value which usually resulted in a voltage drop of 10 mV across the junction since this voltage value has become the reference value at which magnetic tunneling junctions are compared. Then the solenoid source was ramped from a sufficiently low current value up to a high value allowing the magnetic tunneling junction to completely switch between parallel, then an-

tiparallel and again parallel mode. Thereafter the ramp back was recorded to finish the so called "major loop" in which the hysteresis of the magnetic tunneling junction is completely measured. The voltage drop across the barrier was recorded against the magnetic field measured by the hall sensor placed next to the sample. Together with the known current value it so was possible to gain an $R(H)$ curve. To measure the TMR value the minimum and maximum resistance values were taken from a given data set.

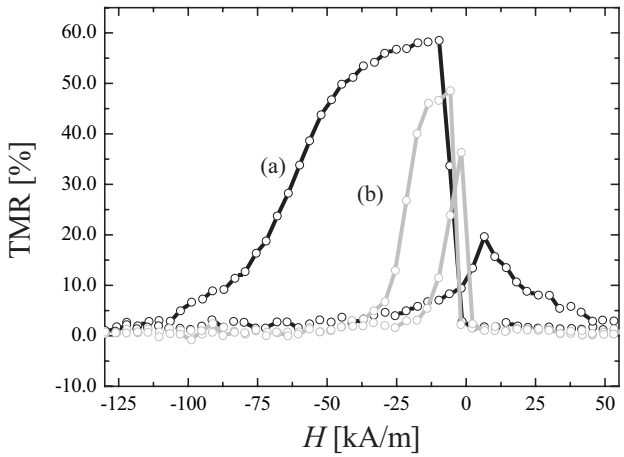


Figure 4.9: *Highest measured TMR value with sample # 3 at (a) $T = 20\ K$ and (b) $T = 300\ K$.*

Fig. 4.9 shows a graph with the TMR value in dependence on the applied external field at two temperatures. This sample showed the highest measured TMR value of 47 % at room temperature. This sample was annealed at 200 °C for 10 min. The asymmetry of the TMR curve seen here reflects the pinning over the exchange-bias effect of the antiferromagnetic FeMn below the bottom electrode CoFe.

Usually TMR values were lower though, regularly lying around $30-35$ % for properly annealed samples[1] and at $20-25$ % for samples as deposited. The latter can be seen in Fig. 4.10 for a wide range of barrier thicknesses from the TMR values of samples corresponding to the barrier value measurements from

[1]The effect of annealing on the TMR value will be shown below

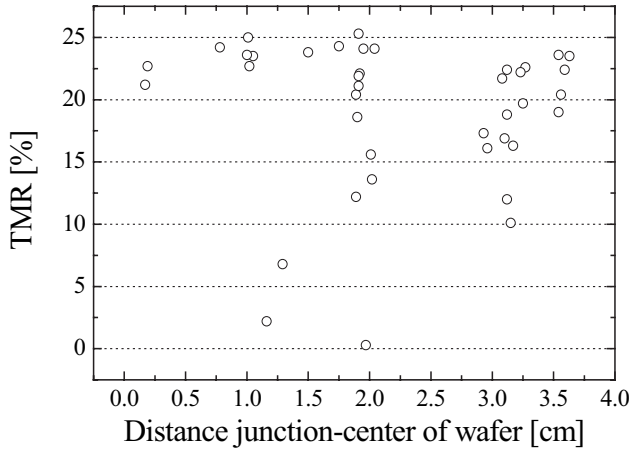


Figure 4.10: *TMR values of junctions distributed over sample # 2. The x-axis refers to the distance of the junction position to the center of the wafer where sputter deposition rates were highest.*

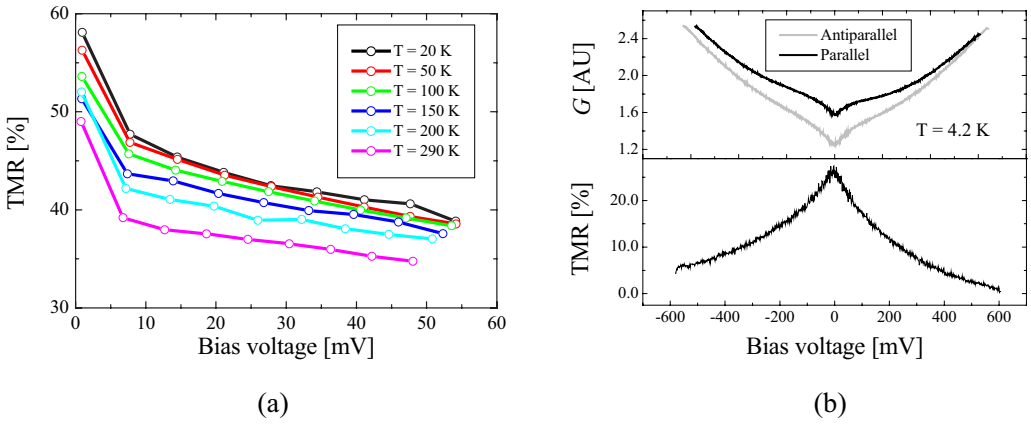


Figure 4.11: *(a) TMR values in dependence on temperature and bias voltage, sample # 3. (b) Dynamic conductance measurement for antiparallel and parallel alignment of the electrode magnetization (top) and calculated TMR curve (bottom), sample # 4.*

Fig. 4.6. Over a whole 4“-wafer surface with a radially changing thickness samples mostly show the same TMR value. Aberrations again pertain to local processing errors that drastically reduce TMR values.

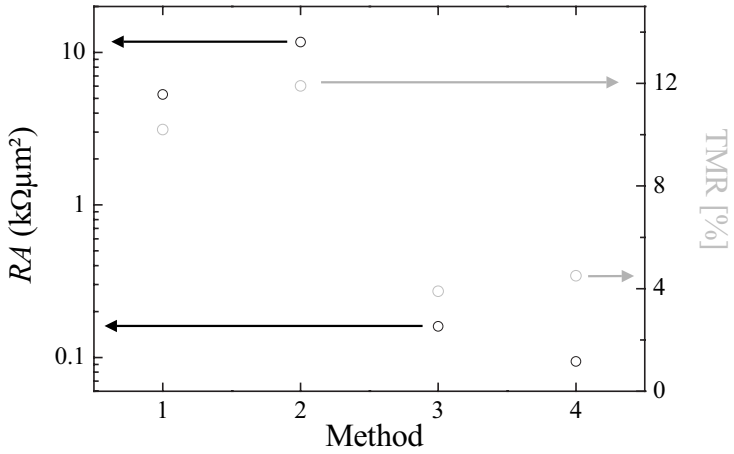


Figure 4.12: *RA products (black circles) and TMR values (red circles) in dependence on oxidation methods. 1 - static, no shutter; 2 - dynamic, no shutter; 3 - static, shutter; 4 - dynamic, no shutter. Measurements performed with samples # 5 at room temperature, oxidation pressure:* 5 *mbar.*

Before these values could be achieved in magnetic tunneling junctions preliminary investigations were performed on the influence of the UV-light oxidation method on the behavior of junctions. Towards this end, the oxidation process of several samples was varied. On one hand, the oxygen supply was used in either dynamic or static mode. This means that the desired end pressure during the oxidation was kept either by constant gas flow (and running pumps) or by the intake of sufficient gas and stopped pumps. On the other hand, the influence of the UV-light was modified by letting the light source illuminate the sample or by placing an aluminium shutter in between. With the latter, possible ozone creation still was possible but UV photons could not reach the sample surface anymore. Fig. 4.12 shows the resistance-area products as well as the TMR values of junctions prepared with these different methods. Clearly visibly the illumination with UV-light increases the resistance by around two orders of magnitude. Brinkman fits show that this is due to an increased barrier thickness and barrier height which leads to the conclusion that the generation of ozone does not play a role in the formation of the barrier. The influence of static vs. dynamic oxidation is of

minor consequence in both cases.

The TMR values which at this preliminary state were way below what was possible in later stages of processing, differ also greatly between the samples illuminated with UV-light or not. Since in all samples the aluminium layer thickness was kept constant the decrease of the TMR value in samples without UV-light can be attributed to underoxidation of the barrier. Remaining metallic aluminium at the interface between the ferromagnetic electrode and the barrier leads to an increased number of spin-flip events, causing the reduction of the TMR value. Table 4.2 recapitulates the junction parameters for this experiment. The temperature and bias-dependence

| Sample # | Oxidation method | Area [$\mu$m$^2$] | $RA$ [k$\Omega\mu$m$^2$] | $t$ [nm] | $\varphi$ [eV] | TMR [%] |
|---|---|---|---|---|---|---|
| #5-1 | static, no shutter | 35.3 | 5.3 | 1.15 | 1.02 | 10.2 |
| #5-2 | dynamic, no shutter | 16.0 | 11.7 | 1.21 | 1.02 | 11.9 |
| #5-3 | static, shutter | 16.0 | 0.16 | 0.95 | 0.75 | 3.9 |
| #5-4 | dynamic, shutter | 4.0 | 0.094 | 0.85 | 0.86 | 4.5 |

Table 4.2: *Junction parameters depending on oxidation method.*

of the TMR effect is visible from Fig. 4.11a. Here, the TMR value was taken from measurements performed at several fixed temperatures and bias voltages. In 4.11b the dynamic conductance was recorded via a lock-in amplifier measurement at two fields corresponding to a parallel respectively antiparallel magnetization of the electrodes. The zero-bias anomaly discussed in chapter 1.6 can be observed in the applicable range of $\pm$150 mV. The TMR curve was directly calculated via $TMR = (G_p(U) - G_{ap}(U))/G_{ap}(U)$.

The influence of annealing on magnetic tunneling junctions can be seen in Fig. 4.13. Here, a sample was characterized directly after patterning and then after annealing processes were performed incrementally at the indicated temperature for each 10 min in ambient air after which the sample was cooled down in a magnetic field of 33 kA/m. The tunneling barrier parameters were

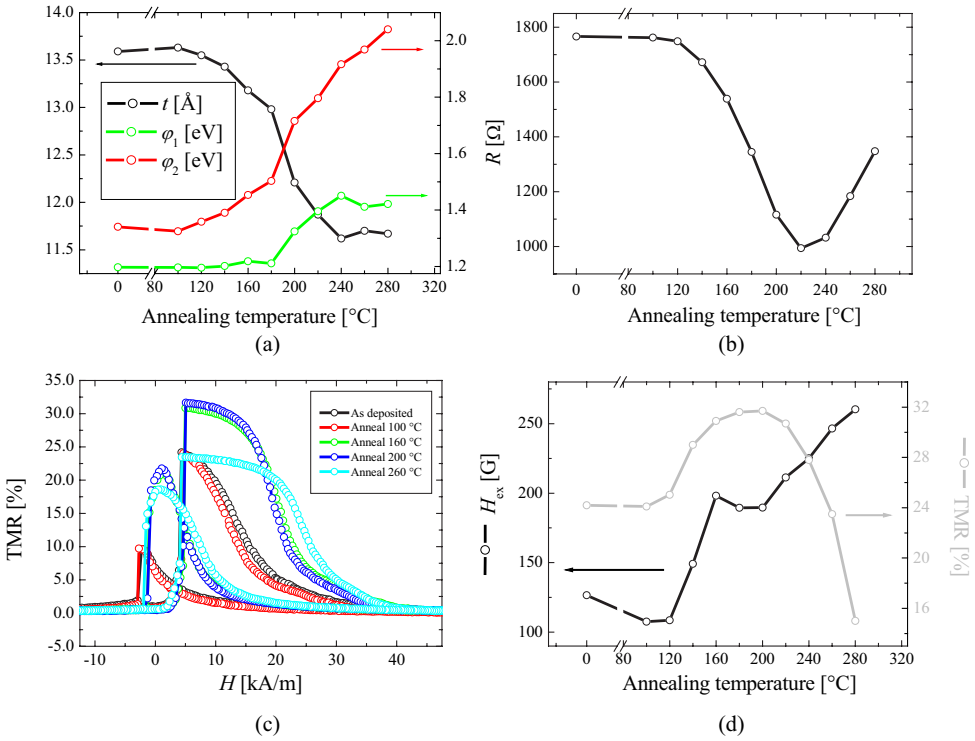


Figure 4.13: *Annealing influence on magnetic tunneling junction properties in sample # 6. (a) Barrier thickness t and barrier potential heights $\varphi_1$, $\varphi_2$ derived from Brinkman fit; $\varphi_1$ corresponds to the barrier height at the top electrode-insulator interface, $\varphi_2$ respectively to the bottom interface. (b) Junction resistance. (c) Selected TMR curves. (d) TMR and exchange bias field values.*

taken from Brinkman fits as usually, the TMR value read from the TMR curves (Fig. 4.13c), and the exchange bias field values $H_{ex}$ from the averaged switching field of both sweep directions. From a temperature of 100 °C an effect of the annealing could be observed: The barrier changed as the thickness decreased and the potential height increased on both interfaces. At the same time the magnetic properties were affected as the TMR value and the exchange bias field increased. The change of the barrier properties can be attributed to a pull-back of excess oxygen which during the oxidation process of the sample formed CoFe oxides. As the sample is heated the excess

oxygen diffuses towards the aluminium, thus reducing the insulator thickness while at the same time increasing the barrier quality which is reflected by the higher barrier height. The increased TMR value shows that this improvement of the barrier also leads to better interfaces as the TMR and thus the spin polarization of the interface region of the CoFe layers is increased. This is readily explainable by the reduction of oxygen sites in these interface regions. These sites form possibly antiferromagnetic Co oxides leading to spin-flip events.

As the annealing temperature is increased to values beyond 200 °C the TMR value begins to recede. This can be traced to the onset of atomic diffusion between individual layers. Diffusion of Co [89] at first degrades the electrode-barrier interface and it is possible that this mechanism also leads to the break-down of the barrier at temperatures around 300 °C. From the still increasing value of the exchange bias field it can be derived that Mn has not yet started diffusion. Literature puts the onset temperature of Mn diffusion at 300 °C [90] which fits with the data presented here.

Additional information on the TMR behavior can be derived from Fig. 4.15b. The plot shows TMR values at room temperature and at 4.2 K depending on annealing history. This data deviates a little bit from the data presented in Fig. 4.13d in that the TMR value there peaked after annealing at 200 °C, while here the TMR still rises after annealing at 250 °C. This should be attributed to the fact that the number of subsequent annealing steps differed: Where sample # 6 from Fig. 4.13 saw eight subsequent annealing steps in the range from 100 to 240 °C, sample # 7 from Fig. 4.15 was heated to 250 °C in just three steps. The resulting difference in complete annealing time which was carried out in ambient air can result in unequal diffusion of air components into the layer system. Nevertheless Fig. 4.15b points out to the fact that even after the low temperature TMR value has reached a maximum (after the 200 °C step), the room temperature TMR value can still increase. Possibly the barrier interface part responsible for the generation of temperature-induced magnons can still be changed after

the interfacial composition responsible for the spin polarization reached an optimal configuration.

A look at the temperature dependence of the conductance $G$ and the TMR allowed insights into the way transport took place over the barrier. As these measurements also were conducted in respect to different annealing states this influence could also be examined in more detail. Fig. 4.14 shows conductance versus temperature plots measured in a sample whose electrodes were magnetized parallel to each other. The three curves were taken for the sample as deposited and after annealing steps of each 10 min at the indicated temperatures and a subsequent cool-down in ambient air in a magnetic field of 33 kA/m.

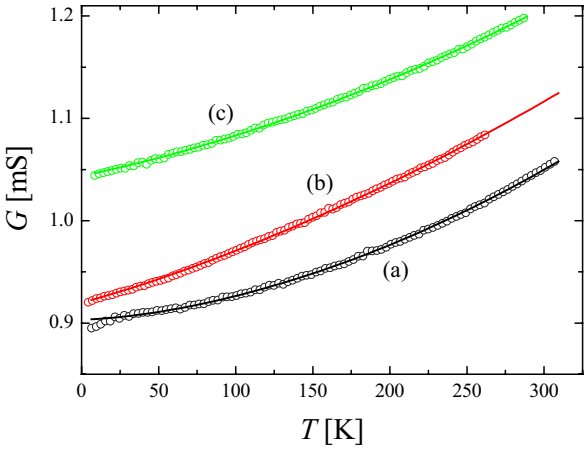


Figure 4.14: *Conductance measurements of sample # 7 at different annealing states. (a) Sample as deposited. (b) After annealing process at 200 °C. (c) After annealing process at 250 °C. Open symbols indicate measurements, solid lines represent the fit discussed in the text.*

Additionally, the TMR value at low temperature (4.2 K) and at room temperature was measured for each step (cf. Fig. 4.15). From the TMR values of Fig. 4.15b the spin polarizations $P_0$ and $P(300\ \mathrm{K})$ were derived from Jullière's equation (1.23), approximating $P_0 \approx P(4.2\ \mathrm{K})$. These two values allowed the determination of the spin wave parameter $\alpha$ via eq. (1.26). Note

that this was not a fit, the temperature dependence of the spin polarization was directly calculated with this equation.

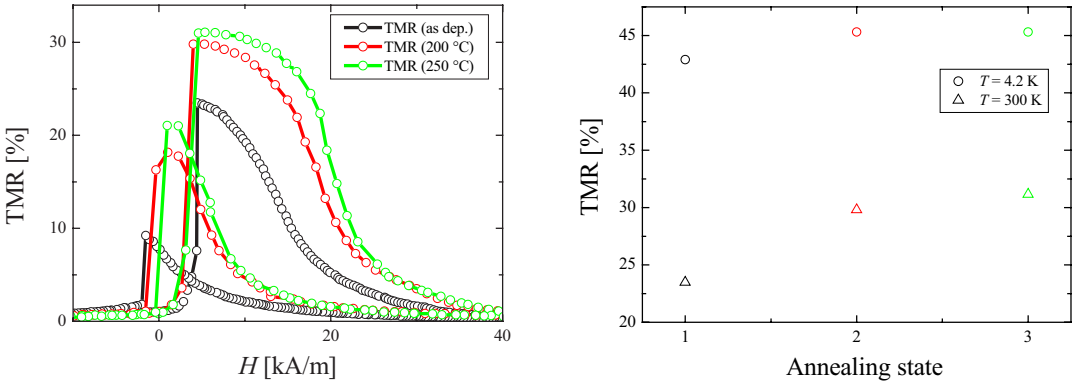


(a) (b)

Figure 4.15: *(a) TMR curves of sample # 7 measured at room temperature for different annealing states as indicated in the legend. (b) TMR values of sample # 7 for different measurement temperatures and annealing states: 1 - as deposited, 2 - annealed at 200 °C, 3 - annealed at 250 °C.*

With the knowledge of $P_0$, the conductivity of the junction with electrodes magnetized parallel to each other can be expressed with eq. (1.25, 1.11):

$$\begin{aligned} G_p(T) &= G^{dir}(T)\left[1+P(T)^2\right]+G^{rest}(T) \\ &= \hat{G}^{dir}\frac{CT}{\sin(CT)}\cdot\left[1+P_0^2\left(1-\alpha T^{3/2}\right)^2\right]+G^{rest}(T). \end{aligned} \tag{4.1}$$

The parameter $\hat{G}^{dir}$ can be calculated directly from $G_p(0\text{ K}) = \hat{G}^{dir}\left[1+P_0^2\right]$, once again assuming that the values for $T = 4.2$ K can be used for zero temperature. $C$ is established with eq. (1.12) and the barrier parameters that are found with a Brinkman fit of the $I$-$U$ curve at $T = 4.2$ K.

With the knowledge of $\hat{G}^{dir}$, $C$, $P_0$, and $\alpha$ the spin-independent part of the conductance $G^{rest}$ can be fitted. Therefore step for step the summands of eq. (1.20) are taken into account. In the case of the data given in Fig. 4.14 the fit was optimal for only one additional tunneling channel $G_2^{hop} = \hat{G}_2 \cdot T^{n_2}$. All parameters of these fits, resistance of the parallel case $R_p$, direct tunneling

conductance contribution $\hat{G}^{dir}$, spin polarizations $P$ at 0 and 300 K, spin wave parameter $\alpha$, and inelastic tunneling channel exponent $n_2$ are found in table 4.3.

| Annealing $T$ [K] | $R_p$(0 K) [Ω] | $\hat{G}^{dir}$ [mS] | $P$(0 K) [%] | $P$(300 K) [%] | $\alpha$ | $n_2$ |
|---|---|---|---|---|---|---|
| as deposited | 1106.7 | 0.7682 | 41.98 | 32.40 | $4.391 \cdot 10^{-5}$ | 1.49 |
| 200 | 1086.5 | 0.7769 | 42.98 | 36.11 | $3.076 \cdot 10^{-5}$ | 1.13 |
| 250 | 957.58 | 0.8817 | 42.95 | 36.71 | $2.796 \cdot 10^{-5}$ | 1.14 |

Table 4.3: *Transport parameters in dependence on annealing process.*

The fit exponent $n_2$ of the inelastic tunneling channel should amount to $n_2 = 4/3$ for tunneling over 2 localized states and $n_2 = 5/2$ for 3 states. As the sample is annealed the measured value decreases from initially around 1.5 down to 1.13. The discrepancy to the literature values could be explained by the fact that the random distribution of localized states in the barrier, an assumption of the Glazman-Matveev model, is actually not given.

## 4.5 Inelastic electron tunneling spectroscopy

IETS measurements were performed by measuring the second derivative of the voltage drop across the barrier in dependence of the current. The second derivative was recorded with the help of the lock-in amplifier in $2f$-mode. For analyzing the measured value $\mathrm{d}^2U/\mathrm{d}I^2$ was transformed via

$$\frac{\mathrm{d}^2I}{\mathrm{d}U^2} = -\left(\frac{\mathrm{d}U}{\mathrm{d}I}\right)^3 \cdot \frac{\mathrm{d}^2U}{\mathrm{d}I^2}. \tag{4.2}$$

This transformation is necessary since results apply for the derivative of the conductance whereas the derivative of the resistance is more easily accessible in a measurement.

To reduce noise and thermal excitations, IET spectra were recorded at $T = 4.2$ K. Samples were characterized for their TMR to know at which field

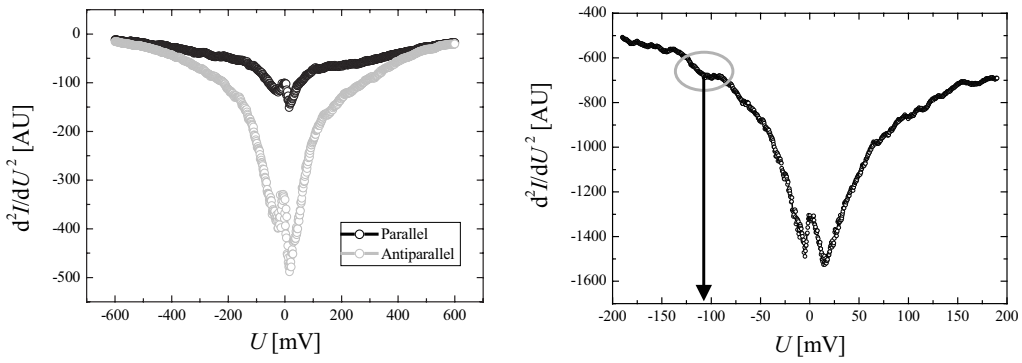


Figure 4.16: *(a) IET spectra of sample # 4 at parallel (P) and antiparallel (AP) alignments of the electrodes. Measured at* $T = 4.2$ *K, modulation peak-to-peak amplitude over junction was* 12 *(P) resp.* 16 *mV (AP). Field for P:* $-150$ *kA/m, AP: first* $-150$*, then* 18 *kA/m. (b) IET spectra of sample #8 at parallel alignment of the electrodes. Temperature and magnetic field as in (a), modulation amplitude* 4 *mV. Marked feature: Al-O stretching mode peak at around* $-110$ *mV.*

values the electrodes are aligned parallel or antiparallel. Then, in either case the first and second derivatives of the current were measured. Fig. 4.16a shows $\mathrm{d}^2I/\mathrm{d}U^2$ as derived from the data via eq. (4.2), the conductance data was already shown in Fig. 4.11. Fig. 4.16b shows data on another sample at parallel alignment of the electrodes. In both cases main features are two strong peaks at around 20 mV that correlate with magnon excitations. In Fig. 4.16b the Al-O stretching mode is visible at $-110$ mV. The fact that this feature is not symmetric as in regard to the current direction shows the differences between the interfaces to the top and bottom electrodes.

The measurement resolution which was given by the modulation amplitudes could not be lowered due to noise issues and so an identification of features beyond those given above was not possible.

## 4.6 Break-down reliability

For breakdown reliability measurements magnetic tunneling junction stacks were deposited in Jülich, patterning and measurements were performed at IMEC, Belgium [57].

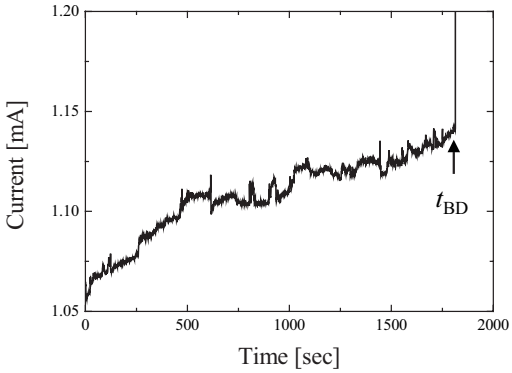


Figure 4.17: *Constant voltage stress measurement of junction of sample # 9 at $U = 1.1$ V.*

Junctions were subjected to constant voltage stress measurements where a constant high bias was applied to a tunneling junction and the tunneling current was measured against time (cf. Fig. 4.17). At the time of break-down $t_{BD}$ an instant current jump can be observed.

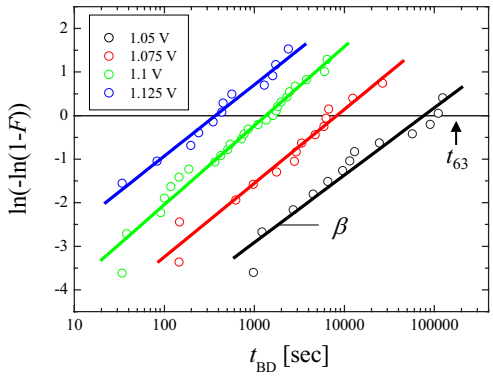


Figure 4.18: *Distribution $F$ of $t_{BD}$ at different junction voltages in sample # 9.*

The cumulative time-to-break-down distribution given by a Weibull function (cf. equation (1.27)) is shown in a Weibull plot in Fig. 4.18. It can be seen that the distributions at the different voltages follow the Weibull function with slope $\beta = 0.8$. At $\ln(-\ln(1-F)) = 0$, 63 % of junctions have broken down, the corresponding values are located at the intersection of the distributions with the zero axis.

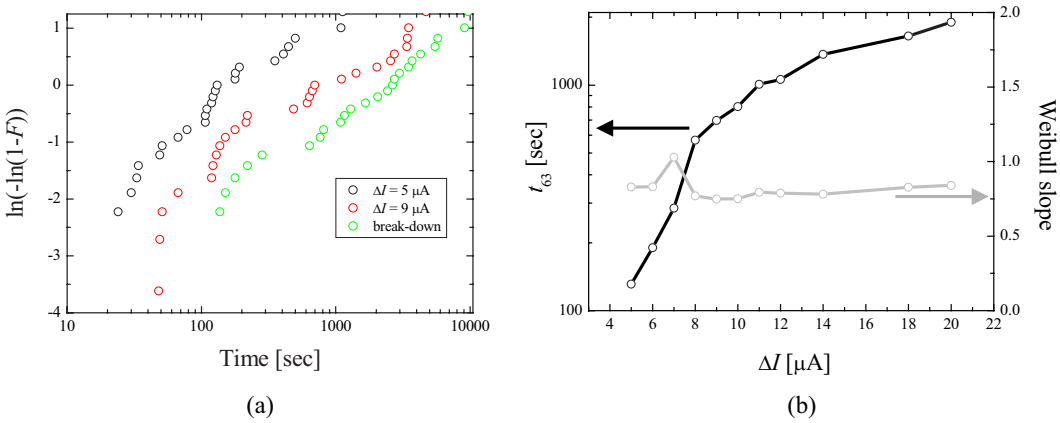


Figure 4.19: *Weibull distribution of pre-break-down current jumps in sample # 9. (a) Distribution of selected current jumps compared with break-down current. (b) $t_{63}$ and Weibull slope $\beta$ of current jumps.*

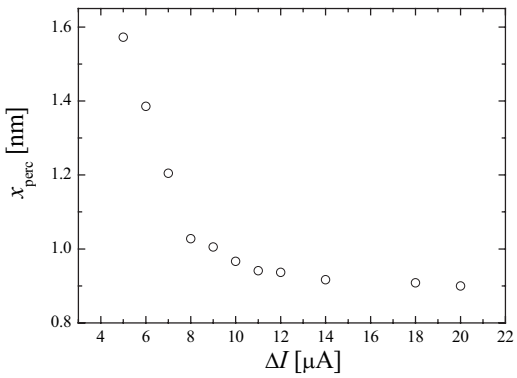


Figure 4.20: *Distance between stress generated trap in barrier and interface in dependence on observed current jumps, sample # 9.*

Before reaching $t_{BD}$ current jumps are observable (cf. Fig. 4.19a) that

follow a Weibull distribution with the same slope of 0.8 (Fig. 4.19b). The fact that $\beta$ remains constant allows the conclusion that the one-trap generation model is valid. The relation between current jump values and the distance of the generated trap from the farther interface is derivable over equations (1.29, 1.30) and leads to the data seen in Fig. 4.20.

# Summary

In this thesis, properties of sputtered magnetic tunneling junctions were investigated. Attention was mainly turned on the insulating barrier whose properties are most important for the performance of a magnetic tunneling junction especially when considering memory applications. The numerous fabrication details that entail these properties were found out to be rather robust against variations. Over a large range of barrier thickness the UV-light enhanced oxidation process yielded similar TMR values over a wide range of barrier thicknesses. Apart from barrier properties and TMR value magnetic properties like switching could be adjusted by annealing processes. The accidental use of a wrong alloy instead of Permalloy skewed the switching and the exchange-biasing but overall was not critical.

The usual behavior of magnetic tunneling junctions as it is known from results with plasma-oxidized barriers could be reproduced. TMR values of usually more than 30% at room temperature matched and resistance-area products could be kept much lower at values down to a few $k\Omega\mu m^2$. The temperature stability against annealing of the junctions presented here was lower than that from other groups. TMR values started decreasing after annealing steps at temperatures beyond 200 °C were performed. This could possibly be improved if IrMn was employed instead of FeMn as this material starts diffusion at higher temperatures.

Transport processes across the tunneling barrier were examined in the framework of the Glazman-Matveev model. Here, certain shortcomings were observed. The inelastic part of the conductance could not be readily ex-

plained by tranport over chains of localized states since the temperature dependence was not strong enough. Therefore, it seems that the oxide prepared in this work does not show as high a defect density as is known from comparable amorphous barriers (like a-Si) that follow the Glazman-Matveev laws very well.

Other important characteristics of the UV-light oxidized barrier for the usage in memory applications were investigated. To get an understanding of the life-time of a magnetic tunneling junction, the break-down stability of the aluminium oxide was examined. From the statistic distribution a model of stress-induced single trap generation leading to the break-down was derived. IET spectra showed that there exist excitations at the interface corresponding to electrical magnon energies as well as a barrier induced Al-O stretching mode.

# Bibliography


[1] P. Grünberg *et al.*, Phys. Rev. Lett. **57**, 2442 (1986).

[2] G. Binasch *et al.*, Phys. Rev. B **39**, 4828 (1989).

[3] M. Jullière, Phys. Lett. A **54**, 225 (1975).

[4] T. Miyazaki and N. Tezuka, J. Magn. Magn. Mater. **139**, L231 (1995).

[5] M. Durlam *et al.*, IEEE J. Solid-State Circuits **38**, 769 (2003).

[6] J. Frenkel, Phys. Rev. **36**, 1604 (1930).

[7] A. Sommerfeld and H. Bethe, *Handbuch der Physik von Geiger und Scheel* (Julius-Springer-Verlag, Berlin, 1933).

[8] I. Giaever and K. Megerle, Phys. Rev. **122**, 1101 (1961).

[9] C.B. Duke, *Tunneling in solids*, 1st ed. (Academia Press, New York, 1969).

[10] E.L. Wolf, *Principles of electron tunneling spectroscopy*, 1st ed. (Oxford Univ. Press, New York, 1985).

[11] F. Schwabl, *Quantenmechanik*, 2nd ed. (Springer, Heidelberg,1990).

[12] M.H. Cohen *et al.*, Phys. Rev. Lett. **8**, 316 (1962).

[13] J.G. Simmons, J. Appl. Phys. **34**, 1793 (1963).

[14] J.G. Simmons, J. Appl. Phys. **34**, 2581 (1963).

[15] W.F. Brinkman *et al.*, J. Appl. Phys. **41**, 1915 (1970).

[16] Y. Xu *et al.*, Phys. Rev. B **52**, 2843 (1995).

[17] C.H. Shang *et al.*, Phys. Rev. B **58**, 2917 (1998).

[18] A.I. Larkin and K.A. Matveev, Sov. Phys. JETP **66**, 580 (1987).

[19] J. Wingbermühle, Ph.D. thesis, Forschungszentrum Jülich, Germany (2002).

[20] L.I. Glazman and R.I. Shekter, Sov. Phys. JETP **67**, 163 (1988).

[21] Y. Xu, Ph.D. thesis, Stanford University, USA (1992).

[22] L.I. Glazman and K.A. Matveev, Sov. Phys. JETP **67**, 1276 (1988).

[23] N.F. Mott and E.A. Davis, *Electronic processes in noncrystalline materials*, 2nd ed. (Oxford Univ. Press, New York, 1979).

[24] R.C. Jaklevic and J. Lambe, Phys. Rev. Lett. **17**, 1139 (1966).

[25] M. Liehr, Ph.D. thesis, RWTH Aachen, Germany (1982).

[26] R.J.M. van de Veerdonk *et al.*, J. Magn. Magn. Mat. **198**, 152 (1999).

[27] Y. Ando *et al.*, J. Appl. Phys. **93**, 7023 (2003).

[28] N.F. Mott, Adv. Phys. **13**, 325 (1964).

[29] R. Meservey *et al.*, Phys. Rev. Lett. **25**, 1270 (1970).

[30] J.S. Moodera *et al.*, Annu. Rev. Mater. Sci. **29**, 381 (1999).

[31] H.-J. Elmers, *Magnetische Schichtsysteme in Forschung und Anwendung* (Forschungszentrum Jülich, Jülich, 1999).

[32] P. Bruno, *Physical origins and theoretical models of magnetic anisotropy* (Forschungszentrum Jülich, Jülich, 1993).

[33] G. Bertotti, *Hysteresis in Magnetism* (Academic Press, San Diego, 1988).

[34] D.E. Bürgler *et al.*, *Handbook of Magnetic Materials*, Vol. 13 (Elsevier, 2001).

[35] P. Grünberg and D.T. Pierce, *Encyclopedia of Materials: Science and Technology* (Elsevier, 2001).

[36] L. Néel, C. R. Acad. Sci. **255**, 1676 (1962).

[37] W.H. Meiklejohn and C.P. Bean, Phys. Rev. **102**, 1413 (1956).

[38] J. Nogués and I.K. Schuller, J. Magn. Magn. Mat. **192**, 203 (1999).

[39] A.P. Malozemoff, Phys. Rev. B **35**, 3679 (1987).

[40] T.C. Schulthess and W.H. Butler, Phys. Rev. Lett. **81**, 4516 (1998).

[41] R. Nakatani *et al.*, Jpn. J. Appl. Phys. **33**, 133 (1994).

[42] O. Allegranza and M.M. Chen, J. Appl. Phys. **73**, 6218 (1993).

[43] J.C. Slonczewski, Phys. Rev. B **39**, 6995 (1989).

[44] J.M. MacLaren *et al.*, Phys. Rev. B **56**, 11827 (1997).

[45] J. Zhang and R.M. White, J. Appl. Phys. **83**, 6512 (1998).

[46] J. Zhang, Phys. Rev. Lett. **79**, 3744 (1997).

[47] J. Wingbermühle *et al.*, J. Appl. Phys. **92**, 7261 (2002).

[48] T. Hagler *et al.*, J. Appl. Phys. **89**, 7570 (2001).

[49] R. Meservey and P.M. Tedrow, Phys. Rep. **238**, 173 (1994).

[50] J. Inouse and S. Maekawa, J. Magn. Magn. Mater. **198-199**, 167 (1999).

[51] R. Degraeve, Ph.D. thesis, K.U. Leuven, Belgium (1998).

[52] J.H. Stathis, Proc. Int. Reliability Physics Symposium, 132 (2001).

[53] J. Das, Ph.D. thesis, K.U. Leuven, Belgium (2003).

[54] K.F. Schuegraf and C. Hu, J. Appl. Phys. **76**, 3695 (1994).

[55] D.J. DiMaria *et al.*, J. Appl. Phys. **73**, 3367 (1993).

[56] T. Nigam *et al.*, Proc. Int. Reliability Physics Symposium, 62 (1998).

[57] J. Das *et al.*, J. Appl. Phys. **94**, 2749 (2003).

[58] K.-H. Gundlach and P. Schnupp, Zeitschr. f. angew. Phys. **21**, 468 (1966).

[59] R.M. Hill and L.A. Dissado, J. Phys. C: Solid Sate Phys. **16**, 2145 (1983).

[60] H.A.M. de Gronckel *et al.*, Appl. Phys. A *70*, 435 (2000).

[61] K.H. Kingdon and I. Langmuir, Phys. Rev. **22**, 148 (1923).

[62] J.A. Thornton, J. Vac. Sci. Tech. A **15**, 171 (1978).

[63] B. Chapman, *Glow Discharge Processes* (Wiley & Sons, New York, 1980).

[64] J.S. Moodera *et al.*, Appl. Phys. Lett. **70**, 3050 (1997).

[65] J.S. Moodera and L. Kinder, J. Appl. Phys. **79**, 4724 (1996).

[66] N. Cabrera and N.F. Mott, Rep. Progr. Phys. **12**, 163 (1949).

[67] M. Martin *et al.*, Thin Solid Films **250**, 61 (1994).

[68] E.Y. Chen *et al.*, J. Appl. Phys. **87**, 6061 (2000).

[69] H. Tsuge and T. Mitsuzuka, Appl. Phys. Lett. **71**, 3296 (1997).

[70] J. Wang *et al.*, J. Appl. Phys. **93**, 8367 (2002).

[71] M. Ronay and E.-E. Latta, Phys. Rev. B **27**, 1605 (1983).

[72] H. Kroger *et al.*, Appl. Phys. Lett. **39**, 280 (1981).

[73] J.L. Miles and P.H. Smith, J. Electrochem. Soc. **110**, 1240 (1963).

[74] J.S. Moodera *et al.*, Phys. Rev. Lett. **74**, 3273 (1995).

[75] H. Kyung, J.H. Lee *et al.*, Phys. Stat. Sol. A **191**, 296 (2002).

[76] N. Cabrera, Phil. Mag. **40**, 175 (1949).

[77] L. Fritzsch *et al.*, Physica C **296**, 319 (1998).

[78] P. Rottländer, Ph.D. thesis, Forschungszentrum Jülich, Germany (1999).

[79] P. Rottländer *et al.*, J. Appl. Phys. **87**, 6067 (2000).

[80] P. Rottländer *et al.*, J. Magn. Magn. Mater. **210**, 251 (2000).

[81] U. May *et al.*, Appl. Phys. Lett. **78**, 2026 (2001).

[82] M. Covington *et al.*, Appl. Phys. Lett. **76**, 3965 (2000).

[83] S. Schneider, Ph.D. thesis, Forschungszentrum Jülich, Germany, to be published.

[84] R. Schmitz, Ph.D. thesis, Forschungszentrum Jülich, Germany (2001).

[85] Y. Endoh and Y. Ishikawa, J. Phys. Soc. Jpn. **30**, 1614 (1971).

[86] C. Loch, Ph.D. thesis, Universität Kassel, Germany (1999).

[87] H.H. Kohlstedt, private communication.

[88] R.C. Sousa *et al.*, J. Appl. Phys. **85**, 5258 (1999).

[89] J. Schmalhorst *et al.*, J. Appl. Phys. **91**, 7478 (2002).

[90] J.H. Lee *et al.*, J. Appl. Phys. **92**, 6241 (2002).

[91] C. Jia, *Investigation of thin films, heterostructures, and devices of ceramic superconductors by means of high-resolution electron-microscopy*, (Forschungszentrum Jülich, Jülich, 1993).

[92] Y. Ando *et al.*, J. Phys. D **35**, 2415 (2002).

[93] H. Kubota, private communication.

[94] A. Barone, *Principles and applications of superconducting quantum interference devices*, (World Scientific, Singapore, 1992).

[95] S. Stein, *Magnetoelektronik-Meßprogramm*, LABVIEW software (2000).

# Danksagung

Eine Vielzahl an Menschen hat mir geholfen und dazu beigetragen, diese Arbeit fertig zu stellen. Es ist wohl unmöglich, jedem einzelnen zu danken, aber die Hauptbeteiligten möchte ich hier nennen. Mein herzlicher Dank gilt:

Meinem Doktorvater und Betreuer Hermann Kohlstedt. Mit seiner lockeren Art der Anleitung, ständigen Bereitschaft, im Labor oder am Schreibtisch mit einzugreifen und der Ermöglichung, einen Teil der Doktorarbeit in Japan durchzuführen, hat er mein Forschungsleben in großer Weise bereichert. Nicht zu vergessen seien auch die feucht-fröhlichen Grillabende bei ihm und das eine oder andere Fässchen von ihm, die das „Kohlstedt-Team“ so hinter sich hat.

Herrn Professor Rainer Waser für die jahrelange Unterstützung durch Gewährung der Arbeitsstelle und -mittel im Institut für Elektrokeramische Materialien.

Für die Übernahme des Korreferats meiner Dissertation Herrn Professor Hans Micklitz.

Für die kurzfristige Bereitwilligkeit zur Übernahme des Prüfungsvorsitzes Herrn Professor Erwin Müller-Hartmann.

Herrn Dr. Rolf Schmitz, der mich in die Fabrikation und Charakterisierung der Tunnelkontakte eingearbeitet hat, mich in die meisten Anlagen eingewiesen hat und durch seine freundliche Mitarbeit für einen guten Einstieg

sorgte.

Herrn Dr. Jörg Wingbermühle für die Zusammenarbeit bei der Interpretation der temperaturabhängigen Transportmessungen.

Professor Peter Grünberg, Herrn Dr. Daniel Bürgler, Herrn Dr. Rashid Gareev, Herrn Michael Breidbach, Herrn Thorsten Damm und Herrn Lars Pohlmann für Diskussionen und ständige Hilfsbereitschaft bei „magnetischen Problemen“.

Meinen (Ex-)Mitdoktoranden Dr. Julio Rodriguez, Andreas Gerber und Martin Weides für die niemals langweilige Büro- und Laboratmosphäre, die hilfreiche Unterstützung, wozu auch Verpflegung und zahlreiche Wartungsarbeiten an der Sputteranlage gehören, und viele interessante Tage und Abende in Jülich und in Köln.

Herrn Stefan Schneider für Hilfestellungen und die Einweisung in die RIBE.

Herrn Dr. Amitesh Paul für die XRD-Messungen sowie die vielen Diskussionen zum Stand der Sputteranlage, Herrn Dr. Chunlin Jia für die Erstellung der HRTEM-Aufnahmen sowie Herrn Dr. Rob Arons für die Einarbeitung in das SQUID-Magnetometer.

Herrn Holger John für die Einweisung in die Reinraumnutzung und jede Menge Kaffee.

Den Herren Bernd Hermanns, Hermann Bierfeld, Hans Haselier, Reinert Schreiber und Franz-Josef Köhne für Unterstützung bei einer Vielzahl technischer Schwierigkeiten.

Den Herren Ralph Otto und Kurt Hirtz stellvertretend für die prompte und gute Arbeit der elektrischen und mechanischen Werkstatt.

Frau Mona Nonn und Frau Steffi Bunte vom ISG für die Arbeiten an

Maskenherstellung und Säge.

Frau Maria Garcia für die freundliche Betreuung in allen Sekretariatsangelegenheiten.

Herrn Prof. Reinhold Kleiner, Dr. Dieter Kölle, Timo Nachtrab und Dr. Edward Goldobin für den Gastaufenthalt an der Universität Tübingen.

I thank Dr. Johan Das from the IMEC in Leuven, Belgium for the cooperation on the bias stress measurements.

Many thanks go to Professor Terunobu Miyazaki of the Tohoku University in Sendai, Japan for enabling me the great stay in Japan and letting me work in his lab.

I am also indebted to Dr. Hitoshi Kubota for the help, guidance, and simply enough, many translations that made the planning and the time in Sendai so enjoyable. Also, thanks for all the discussions and the continued cooperation!

From the crew in Sendai, finally I also want to thank Mr. Takeharu Kato for the introduction to the sputtering and STM system at the Tohoku University and the *long* measurements made together.

Dem Deutschen Akademischen Austauschdienst gebührt mein Dank für die Gewährung eines Stipendiums für den Aufenthalt in Japan.

Nach dem Dank für die zumeist wissenschaftliche Unterstützung bin ich aber auch für moralische Unterstützung ganz besonders dankbar, die mir mit großer Geduld und viel Liebe meine Eltern, Dr. Peter und Dagmar Stein, meine Geschwister Gregor, Jasper und Deborah Stein und ganz besonders meine Freundin Andrea Wendt entgegenbrachten.

# Erklärung

Ich versichere, dass ich die von mir vorgelegte Dissertation selbständig angefertigt, die benutzten Quellen und Hilfsmittel vollständig angegeben und die Stellen der Arbeit - einschließlich Tabellen, Karten und Abbildungen -, die anderen Werken im Wortlaut oder dem Sinn nach entnommen sind, in jedem Einzelfall als Entlehnung kenntlich gemacht habe; dass diese Dissertation noch keiner anderen Fakultät oder Universität zur Prüfung vorgelegen hat; dass sie - abgesehen von unten angegebenen Teilpublikationen - noch nicht veröffentlicht worden ist sowie, dass ich eine solche Veröffentlichung vor Abschluss des Promotionsverfahrens nicht vornehmen werde. Die Bestimmungen dieser Promotionsordnung sind mir bekannt. Die von mir vorgelegte Dissertation ist von Priv.-Doz. Dr. H. H. Kohlstedt betreut worden.

## Veröffentlichungen

- "Magnon scattering and tunneling through localized states in magnetic tunnel junctions",
  Journal of Applied Physics **92**, 7261 (2002) (J. Wingbermühle, S. Stein, H. Kohlstedt)

- "Statistical model for prebreakdown current jumps and breakdown caused by single traps in magnetic tunnel junctions",
  Journal of Applied Physics **94**, 2749 (2003) (J. Das, R. Degraeve, G. Groeseneken, S. Stein, H. Kohlstedt, G. Borghs, J. De Boeck)

## Konferenzbeiträge

- "Influence of spin-polarized injection currents on magnetic tunnelling junctions",
  Joint European Magnetic Symposia 2001, Grenoble, Frankreich (S. Stein, H. Kohlstedt, R. Waser)

- "Spin-injection effects in three terminal magnetic tunnelling junctions",
  Fall meeting 2001 of the Materials Reserach Society, Boston, USA (S. Stein, H. Kohlstedt, R. Waser)

- "Magnon scattering and tunneling through localized states in magnetic tunnel junctions",
  SpinTech II 2003, Bruges, Belgium (S. Stein, M. Weides, C.L. Jia, H. Kohlstedt, D. Bürgler, P. Grünberg, R. Waser)

Köln, im November 2003

Simon Stein

Forschungszentrum Jülich
*in der Helmholtz-Gemeinschaft*

Jül-4123
März 2004
ISSN 0944-2952